

ALMA OBSERVATION OF NGC 5135: THE CIRCUMNUCLEAR CO (6–5) AND DUST CONTINUUM EMISSION AT 45 PARSEC RESOLUTION*

TIANWEN CAO^{1,2,3,4}, NANYAO LU¹, C. KEVIN XU¹, YINGHE ZHAO^{5,6,7}, VENU MADHAV KALARI⁸, YU GAO⁹, VASSILIS CHARMANDARIS^{10,11}, TANIO DIAZ SANTOS¹², PAUL VAN DER WERF¹³, CHEN CAO^{14,15}, HONG WU^{2,3}, HANA E INAMI¹⁶, AARON EVANS^{17,18}

Accepted for publication in APJ; September 18, 2018

ABSTRACT

We present high-resolution ($0.17'' \times 0.14''$) Atacama Large Millimeter/submillimeter Array (ALMA) observations of the CO (6–5) line, and $435 \mu\text{m}$ dust continuum emission within a $\sim 9'' \times 9''$ area centered on the nucleus of the galaxy NGC 5135. NGC 5135 is a well-studied luminous infrared galaxy that also harbors a Compton-thick active galactic nucleus (AGN). At the achieved resolution of $48 \times 40 \text{ pc}$, the CO (6–5) and dust emissions are resolved into gas “clumps” along the symmetrical dust lanes associated with the inner stellar bar. The clumps have radii between $\sim 45\text{--}180 \text{ pc}$ and CO (6–5) line widths of $\sim 60\text{--}88 \text{ km s}^{-1}$. The CO (6–5) to dust continuum flux ratios vary among the clumps and show an increasing trend with the $[\text{Fe II}]/\text{Br-}\gamma$ ratios, which we interpret as evidence for supernova-driven shocked gas providing a significant contribution to the CO (6–5) emission. The central AGN is undetected in continuum, nor in CO (6–5) if its line velocity width is no less than $\sim 40 \text{ km s}^{-1}$. We estimate that the AGN contributes at most 1% of the integrated CO (6–5) flux of $512 \pm 24 \text{ Jy km s}^{-1}$ within the ALMA field of view, which in turn accounts for $\sim 32\%$ of the CO (6–5) flux of the whole galaxy.

Keywords: galaxies: active – galaxies: starburst – galaxies: general – galaxies: nuclei – galaxies: ISM

1. INTRODUCTION

Luminous infrared galaxies (LIRGs; $L_{\text{IR}}^{[8\text{--}1000 \mu\text{m}]} \gtrsim 10^{11} L_{\odot}$), whose space density exceeds that of optically selected starburst and Active Galactic Nucleus (AGN) host galaxies at comparable bolometric luminosities (Soifer et al. 1987), consist of isolated galaxies, galaxy pairs, interacting galaxy systems and advanced mergers (Sanders & Mirafbel 1996; Wang et al. 2006). LIRGs in the later stages of evolution tend to contain a rich amount of molecular gas in the galaxy nuclear region (Sanders et al. 1986), and have a higher fraction of AGNs compared with less luminous galaxies (Sanders & Mirafbel 1996). Detailed investigations of the physical properties, AGN-starburst connection, and gas inflow/outflow in representative LIRGs in the local Universe are critical to our understanding of galaxy evolution because LIRGs are the dominant contributors to the cosmic star formation (SF) at $z \gtrsim 1$ (Le Floch et al. 2005; Caputi et al. 2007; Magnelli et al. 2009, 2011; Gruppioni et al. 2013).

The CO emission lines from low- J transitions, such as CO (1-0) at 2.6 mm and CO (2-1) at 1.3 mm, have been widely used to trace the molecular gas content in LIRGs (Solomon & Sage 1988; Sanders et al. 1991; Solomon et al. 1997; Bryant & Scoville 1999; Gao & Solomon 1999; Evans et al. 2002). However, based on the data taken with the SPIRE Fourier Transform Spectrometer (FTS; Griffin et al. 2010) onboard the *Herschel Space Observatory* (*Herschel*; Pilbratt et al. 2010) on a flux-limited sample of 123 LIRGs from the Great Observatories All-Sky LIRGs Survey (GOALS; Armus et al. 2009), Lu et al. (2014, 2017) showed that the mid- J CO emission (i.e., $4 < J < 10$) from warm and dense molecular gas correlates linearly with the star formation rate (SFR) on galactic scale for LIRGs over a wide range of L_{IR} and far-infrared (FIR) color. Therefore, the heating mechanism for the

¹ Chinese Academy of Sciences South America Center for Astronomy, National Astronomical Observatories, Chinese Academy of Sciences, Beijing 100101, China; twcao@bao.ac.cn

² Key Laboratory of Optical Astronomy, National Astronomical Observatories, Chinese Academy of Sciences, Beijing 100101, China

³ School of Astronomy and Space Science, University of Chinese Academy of Sciences, Beijing 100049, China

⁴ Instituto de Astrofísica, Pontificia Universidad Católica de Chile, Av. Vicuña Mackenna 4860, 7820436 Macul, Santiago, Chile

⁵ Yunnan Observatories, Chinese Academy of Sciences, Kunming 650011, China

⁶ Key Laboratory for the Structure and Evolution of Celestial Objects, Chinese Academy of Sciences, Kunming 650011, China

⁷ Center for Astronomical Mega-Science, CAS, 20A Datun Road, Chaoyang District, Beijing 100012, China

⁸ Departamento de Astronomía, Universidad de Chile, Casilla 36-D, Correo Central, Santiago, Chile

⁹ Purple Mountain Observatory/Key Lab of Radio Astronomy, 8 Yuanhua Road, 210034 Nanjing, China

¹⁰ Department of Physics, University of Crete, GR-71003 Heraklion, Greece

¹¹ IAASARS, National Observatory of Athens, GR-15236, Pen-teli, Greece

¹² Ncleo de Astronomia de la Facultad de Ingeniería, Universidad Diego Portales, Av. Ejército Libertador 441, Santiago, Chile

¹³ Leiden Observatory, Leiden University, P.O. Box 9513, 2300 RA Leiden, The Netherlands

¹⁴ School of Space Science and Physics, Shandong University, Weihai, Weihai, Shandong 264209, China

¹⁵ Shandong Provincial Key Laboratory of Optical Astronomy & Solar-Terrestrial Environment, Weihai, Shandong 264209, China

¹⁶ Univ. Lyon, Univ. Lyon1, ENS de Lyon, CNRS, Centre de Recherche Astrophysique de Lyon (CRAL) UMR 5574, 69230 Saint-Genis-Laval, France

¹⁷ Department of Astronomy, University of Virginia, Charlottesville, VA 22903-2325, USA

¹⁸ National Radio Astronomy Observatory, 520 Edgemont Road, Charlottesville, VA 22903-2475, USA

* The National Radio Astronomy Observatory is a facility of the National Science Foundation operated under cooperative agreement by Associated Universities, Inc.

warm dense gas that gives rise to the mid- J CO line emission should ultimately derive the energy from the same SF process that powers the dust emission. There is not yet a firm consensus on this heating mechanism. Apparently different heating mechanisms are favored from analyses of the CO emission line spectra of individual galaxies, including far-UV photon heating (e.g., Rigopoulou et al. 2013), heating by cosmic rays enhanced by supernovae (SNe; e.g., Bradford et al. 2003), and heating by shocks that may or may not be powered by SNe (e.g., Kamenetzky et al. 2012; Rangwala et al. 2011; Nikola et al. 2011; Meijerink et al. 2013; Pellegrini et al. 2013; Rosenberg et al. 2014). The X-ray photons from an AGN can heat the surrounding dense gas very effectively (e.g., Spaans & Meijerink 2008). However, Lu et al. (2017) argued that the CO line emission associated with any AGN gas heating may peak at $J > 10$. As a result, the mid- J CO line emission is always dominated by SF.

With the Atacama Large Millimeter/submillimeter Array (ALMA; Wootten & Thompson 2009), it is now possible to obtain high-resolution mid- J CO line and dust continuum images of the nuclei of nearby LIRGs to investigate whether the *Herschel* results above still hold true at physical scales down to the typical size of giant molecular clouds (GMCs; i.e., ~ 40 pc, Kawamura et al. 2009), and whether one can rule out some of the gas heating mechanisms proposed. To this end, we have carried out a number of ALMA Band-9 observations over time, to image simultaneously the CO (6-5) line emission (the rest frequency $\nu_{\text{rest}} = 691.473$ GHz) and its underlying dust continuum at $435 \mu\text{m}$ in the nuclear regions of a set of carefully selected, representative LIRGs from our *Herschel* FTS sample. The targets observed include NGC 34 (Xu et al. 2014) and NGC 1614 (Xu et al. 2015), two advanced mergers with a warm FIR color; NGC 7130 (Zhao et al. 2016) and NGC 5135 (in this paper), two well-known Seyfert galaxies with a prominent stellar bar; IC 5179 (Zhao et al. 2017), an isolated, unbarred galaxy with a compact nuclear starburst; and CGCG 049-057 with a high-surface density nuclear SF disk (Cao et al., in preparation). The linear resolutions (R_{linear}) achieved range from 100 pc in the early observation of NGC 34 to 34 pc in the case of IC 5179. Three additional LIRGs in our FTS sample also have ALMA CO (6-5) images in the literature: Arp 220 ($R_{\text{linear}} \sim 165$ pc; Wilson et al. 2014; Rangwala et al. 2015), IRAS 13120-5453 ($R_{\text{linear}} \sim 165$ pc; Sliwa et al. 2017), and NGC 1068 ($R_{\text{linear}} \sim 4$ pc; García-Burillo et al. 2014, 2016). ALMA CO (6-5) images also exist for two nearby, but non-LIRG galaxies: NGC 1377 (Aalto et al. 2017) and Centaurus A (Espada et al. 2017).

At a distance of 59 Mpc ($1''$ corresponds to 281 pc) and with a fairly face-on disk, NGC 5135 is a well studied LIRG with $L_{\text{IR}} = 10^{11.33} L_{\odot}$ and a moderately warm FIR color of 0.54 (in terms of the 60-to-100 μm flux density ratio; Armus et al. 2009). The galaxy not only displays a powerful circumnuclear starburst over a region of ~ 1 kpc in diameter (González Delgado et al. 1998; Bedregal et al. 2009) but also harbors a highly obscured Seyfert 2 nucleus (Levenson et al. 2004; Phillips et al. 1983; Turner et al. 1997). It is therefore an ideal target for high-resolution ALMA observations to separate the circumnuclear SF from the AGN. The 6 cm radio continuum emission peaks in an area $\sim 3''$ south of the nucleus based on a

Very Large Array (VLA) observation by Ulvestad & Wilson (1989), presumably tracing the supernova remnants (SNRs) from a previous starburst. The high-resolution *Hubble Space Telescope* (*HST*) UV/optical imaging observations unveiled a large number of young star clusters, between the nucleus and the radio continuum peak (González Delgado et al. 1998), which presumably have partially cleared gas. Furthermore, the high-resolution near- and mid-infrared images (Alonso-Herrero et al. 2006; Díaz-Santos et al. 2008) show patches of strong on-going SF along, but at the downstream side of the dust lanes that are likely associated with the stellar bar (e.g. (Mulchaey & Regan 1997)). An intermediate resolution ($R \sim 3000\text{--}4000$), near-infrared integral-field spectroscopy (Bedregal et al. 2009) confirmed the presence of a high-excitation ionization cone centered on the AGN, based on the [Si VI] $1.96 \mu\text{m}$ line emission, as well as an extended distribution of shocked gas likely powered by SNe, based on the [Fe II] $1.46 \mu\text{m}$ line. Fukazawa et al. (2011) and Singh et al. (2012) obtained broad-band (10–50 keV) X-ray spectra of NGC 5135, demonstrating that the AGN in NGC 5135 is obscured by Compton-thick material. Our ALMA imaging of NGC 5135 presented here provides for the first time the distribution and kinematics of the warm and dense molecular gas as well as the morphology of the $435 \mu\text{m}$ dust emission, at a linear resolution of less than 50 pc in the circumnuclear region of NGC 5135.

In the remainder of the paper, we describe our ALMA observation and data reduction in §2 and present our results in §3. In §4, we discuss the physical implications derived from our data on the circumnuclear SF and the role of the AGN, compare our ALMA images with existing images at other wavelengths, and comment on the most likely heating mechanism for the observed CO (6-5) emission. Thereby allowing us to distinguish between different heating mechanisms, and the role played by SF in giving rise to the mid- J CO emission. Finally, we summarize our results in §5. Throughout this paper, we adopt a distance of 59 Mpc for NGC 5135 (Armus et al. 2009).

2. OBSERVATION AND DATA REDUCTION

The ALMA band-9 observation of NGC 5135 was carried out in the time division mode (with a velocity resolution of $\sim 6.8 \text{ km s}^{-1}$). The four basebands (i.e., Spectral Windows; SPWs 0-3) were centered on sky frequencies of 681.975, 683.736, 678.243 and 680.183 GHz, respectively, with a bandwidth of 1.875 GHz. The observation was performed with the configuration mode C34-5, using 39 12-meter antennae with baselines ranging from 21.3 to 885.6 meters. The total on-target integration time is 21.03 minutes. During the observation, the phase calibration and amplitude were monitored using J1316-3328. Additional observing details can be found in Table 1.

The data were reduced using the Common Astronomical Software Application (CASA) version 4.5 (McMullin et al. 2007). Our primary beam is $\sim 8.8''$ and the Maximum Recoverable Scale (MRS)¹ is $3.5''$. The CO (6-5) line data cube was generated using the data in the SPW covering the sky frequency range of 680.975 to 682.975 GHz. The continuum was estimated by combining the data from the other three SPWs. The calibrated images were cleaned using the Briggs weighting (with the parameter “robust” set to 0.5). The resulting synthesized

beams are nearly identical between the continuum and the line emission and have a full width at half maximum (FWHM) size of $\sim 0.17'' \times 0.14''$ (equivalent to 48×40 pc at the distance to NGC 5135), with the major-axis position angle (north to east) at 111° . All our analyses in this paper use the data after the primary beam correction, whereas all of the figures (except Fig. 6) were produced using data prior to the primary beam correction.

The final spectral cube has a channel width equivalent to 13.5 km s^{-1} in velocity. The channel noise (σ_{ch}) is on the order of 18 mJy beam^{-1} . The total CO (6-5) flux image, as an integration over the barycentric velocities from $3,971$ to $4,157 \text{ km s}^{-1}$, has an r.m.s. noise of $\sim 1.2 \text{ Jy beam}^{-1} \text{ km s}^{-1}$. The continuum image has a noise of $2.2 \text{ mJy beam}^{-1}$. All these noise measurements were done on the data without the primary beam correction. The ALMA absolute flux calibration is estimated to be good to $\sim 10\%$. The astrometric accuracy is better than $0.01''$.

3. RESULTS

3.1. CO (6-5) Line Emission

The four panels in Fig. 1 show respectively the images of the total CO (6-5) emission integrated between the observed velocities of 3971 and 4157 km s^{-1} , the $435 \mu\text{m}$ continuum, the velocity field (i.e., moment 1), and velocity dispersion map (moment 2). Each image roughly covers the ALMA primary beam. The contours overlaid in Fig. 1a and 1b refer to the same total CO (6-5) emission and start at $S/N = 3$.

The CO (6-5) emission detected at $S/N > 3$ appears clumpy and is confined to a few discrete regions along two spiral arm-like features corresponding spatially to the dust lanes seen in the UV and optical (e.g., Muñoz Marín et al. 2007). We mark four separate regions, namely (*a*, *b*, *c*, *d*) which are compact and concentrated in the integrated CO (6-5) map. The region *d* appears more diffuse compared with the other three. The total CO (6-5) flux from the combined four regions in Fig. 1a is $512 \pm 24 \text{ Jy km s}^{-1}$. With a much larger beam of $\sim 31''$, the *Herschel*/FTS observation gives a CO (6-5) flux of $1,617 \text{ Jy km s}^{-1}$ (Lu et al. 2017). Therefore the clump regions in Fig. 1a together account for $\sim 32\%$ of the total CO (6-5) flux of the galaxy. The "missing" line flux could be due to a combination of the line emission outside the ALMA field of view, or possible faint emission at peak surface brightness below our $3\text{-}\sigma$ (i.e., $3.6 \text{ Jy beam}^{-1} \text{ km s}^{-1}$) detection limit, or resolved out on larger scales. We analyze individual clumps in more detail in §4.2.

We set the threshold at $4\text{-}\sigma_{\text{ch}}$, where σ_{ch} is the r.m.s. noise per frequency channel, to obtain the moment 1 and 2 maps. To reveal the kinematics better, the moment 1 and 2 maps, shown respectively in Fig. 1c and 1d, were based on the uv-taper image (the details about the uv-taper image are presented in the last paragraph of this subsection). The velocity scale in Fig. 1c was calculated using the formula $\nu_{\text{obs}} = \nu_{\text{rest}} (1 - V/c)$, where ν_{obs} is the observed CO (6-5) line frequency, *c* the speed of light, and *V* the velocity to calculate. The line velocity ranges

from 3992 to 4140 km s^{-1} . Fig. 1d shows that the line-of-sight velocity dispersion ranges from 10 to 40 km s^{-1} , using only those pixels with $S/N > 4\text{-}\sigma_{\text{ch}}$. The overall kinematic pattern can also be seen in the channel maps displayed in Fig. 2, where the contours from an individual channel of width 13.5 km s^{-1} are overlaid on the grayscale image of the total CO (6-5) flux map shown in Fig. 1a. While the regions *a*, *c*, *d* are mainly confined within a velocity range of 3992 to 4073 km s^{-1} , the region *b* has a range between 4046 and 4127 km s^{-1} . This suggests that the observed velocity pattern is not dominated by a simple rotation within the galaxy disk. In the channel maps, some CO (6-5) clumps break down into smaller clumps (or clouds) in some velocity channels, e.g., the region *a* in the channel centered at $V = 4073 \text{ km s}^{-1}$. These clouds have sizes < 50 pc.

In Fig. 3a and 3b, we reproduced the same images as in Fig. 1a and 1b, respectively, but with a larger effective beam of $0.4'' \times 0.4''$ (equivalent to 112×112 pc) by applying an uv-taper (with the parameter "outertaper" = $0.4''$) to our uv data before imaging. The peak signal of the region *d* is higher than $4\text{-}\sigma$ ($\sigma = 8 \text{ Jy beam}^{-1} \text{ km s}^{-1}$). The total flux of the four regions combined, as defined in Fig. 1, is $841 \pm 45 \text{ Jy km s}^{-1}$. This flux equals 1.6 times the flux from the original ALMA image, and is $\sim 52\%$ of the total flux measured by *Herschel*, confirming that there exists some more diffuse or lower surface brightness CO (6-5) emission within the region of Fig. 1a.

3.2. Dust Continuum Emission

As shown in Fig. 3b, the continuum at $435 \mu\text{m}$ generally coincides with the CO (6-5) line emission in regions *a* and *c* at scales of $0.4''$ (equivalent to 112 pc), which corresponds to an angular size of 114 pc at the distance of NGC 5135. This is consistent with the findings in the other LIRGs we imaged in CO (6-5), i.e., NGC 34, NGC 1614 and NGC 7130 and IC 5179 (Xu et al. 2014, 2015; Zhao et al. 2016, 2017), i.e., at scales $\gtrsim 100$ pc, there is a good spatial correspondence between the CO (6-5) line and its underlying continuum emissions.

However, at scales significantly smaller than 100 pc, there are apparent offsets between the local peaks of the line and continuum emissions in Fig. 1b. This small-scale offset between the line and continuum emissions is also seen in the LIRGs of moderately high nuclear gas surface densities, e.g., IC 5179 (at linear resolution $R_{\text{linear}} \approx 34$ pc; Zhao et al. 2017) and NGC 7130 ($R_{\text{linear}} \approx 70$ pc $\times 40$ pc; Zhao et al. 2016). Furthermore, in both Fig. 1b and 3b, the dust continuum is unusually weak relative to the line emission in the regions *b* and *d*. As argued in Zhao et al. (2016), these differences between the line and dust continuum emissions at small scales can only be understood if the gas and dust are heated by different mechanisms. We discuss this in more detail in §4.3.

By combining the four regions in Fig. 1b, we derived a total flux of $181 \pm 25 \text{ mJy}$ for the $435 \mu\text{m}$ continuum emission. This flux would be 1.6 times higher if we had derived it from the same regions in Fig. 3b.

4. ANALYSIS AND DISCUSSION

4.1. The Central AGN

¹ <https://science.nrao.edu/science/videos/largest-angular-scale-and-maximum-recoverable-scale>

The AGN position can be constrained by the peak of the [Si VI] line emission at $1.96 \mu\text{m}$ in a ground-based observation (Bedregal et al. 2009) and by the peak of the hard X-ray (4-8 keV) emission detected with Chandra (Levenson et al. 2004). The estimated astrometric uncertainty associated with either of these images is on the order of $0.5''$. The VLA 6 cm radio continuum image of Ulvestad & Wilson (1989) has a modest resolution of $0.91'' \times 0.60''$ and an astrometric accuracy of $0.3''$. We overlaid our CO (6-5) contours from Fig. 1a on this radio continuum image in Fig. 4a. As already stated in Sec. 1, the main peak of the 6 cm emission is $\sim 3''$ south of the galaxy nucleus, spatially coincident with the peak of the broad (FWHM = $\sim 513 \text{ km s}^{-1}$) [Fe I] emission (Bedregal et al. 2009). However, there is a minor radio emission peak (10σ) near the anticipated AGN position. We take the position of this radio peak (R.A. = $13^{\text{h}}25^{\text{m}}44^{\text{s}}.02$, Dec. = $-29^{\circ}50'00''.4$; J2000) as the AGN location (i.e., marked by the white cross), with a positional uncertainty of $0.3\text{-}0.5''$. In Fig. 4b, we overlaid the same CO (6-5) contours on the hard X-ray emission.

As shown in Fig. 1a, the CO (6-5) emission is undetected at $4\text{-}\sigma$ level at the AGN position (i.e., integrated over the velocity range of 186 km s^{-1}). This would hold true even if we had lowered the detection threshold to $3\text{-}\sigma$. We assume the AGN-related CO (6-5) emission is confined to an area smaller than our ALMA beam size ($\sim 48 \times 40 \text{ pc}$), then the $3\text{-}\sigma$ flux upper limit is equal to $3 \times (1.2 \text{ Jy km s}^{-1}) = 3.6 \text{ Jy km s}^{-1}$ ($\sigma = 1.2 \text{ Jy beam}^{-1} \text{ km s}^{-1}$).

However, an apparent narrow emission feature at the AGN location is seen at $3\text{-}4 \sigma$ significance over only two velocity channels (i.e., $V = 4019.0$ and 4032.5 km s^{-1}). The image summed over these two velocity channels is presented in Fig. 5a, which shows a peak surface brightness of 33 mJy beam^{-1} (at $5\text{-}\sigma$ significance). The spectrum in Fig. 5b is extracted from a circular aperture of radius = $0.4''$ (= 2.5 times the FWHM of the $3\text{-}\sigma$ surface brightness of the emission in Fig. 5a). Its narrow velocity width of $\sim 40 \text{ km s}^{-1}$ makes it unlikely that this signal is physically associated with the AGN. Nevertheless, considering that the CO (6-5) emission associated with the gas torus of the AGN in NGC 1068 is observed to have only a modest velocity width of $\sim 80 \text{ km s}^{-1}$ (García-Burillo et al. 2016), we defer to a future observation of higher angular resolution to firmly conclude the reality of this narrow CO (6-5) emission. Flux-wise, the narrow CO (6-5) emission in Fig. 5b has a flux of 1.7 Jy km s^{-1} , which is smaller than the $3\text{-}\sigma$ flux upper limit of 3.6 Jy km s^{-1} derived above. Therefore, we conclude that the AGN in NGC 5135 contributes at most 1% of the CO (6-5) flux observed within the ALMA field of view. This is consistent with the *Herschel* finding that the mid- J CO line emission in LIRGs is mainly associated with SF regardless of whether there is an AGN or not (Lu et al. 2017). The fractional contribution of the AGN to the bolometric luminosity of NGC 5135 is about $(24 \pm 6)\%$ (Díaz-Santos et al. 2017). The AGN in NGC 5135 is heavily obscured; the surrounding gas could be heated to a very high temperature by the X-rays associated with the AGN, resulting in a CO spectral line distribution that peaks $J > 10$ (Spaans & Meijerink 2008). Such a scenario seems to be the case in the Seyfert galaxy

NGC 1068: While the high-resolution ALMA imaging shows that the vast majority of the nuclear CO (6-5) emission is associated with the compact circumnuclear ring of SF at a radius of $\sim 100 \text{ pc}$ (García-Burillo et al. 2016), the total nuclear CO emission line spectrum has a distinct component that peaks at $J \sim 16$ (Spinoglio et al. 2012). This hot spectral component of the CO emission is presumably due to the AGN in NGC 1068. The central AGN in NGC 5135 is bright in terms of the $1\text{-}0 \text{ S}(1) 2.12 \mu\text{m}$ H₂ ro-vibrational line (Bedregal et al. 2009) associated with warm molecular gas. Although this line could be excited by different physical processes, including UV-fluorescence (photons); shock fronts (collisions) and X-ray illumination, Bedregal et al. (2009) argued that the excited near-IR H₂ emission is mainly caused by X-ray illumination in the AGN region of NGC 5135. Such an X-ray dominant scenario is also favored based on non-detection of the CO (6-5) emission here.

The $435 \mu\text{m}$ dust continuum is also undetected at the AGN position, with the $3\text{-}\sigma$ flux upper limit equal to 5.4 mJy ($\sigma = 1.8 \text{ mJy beam}^{-1}$; the same method used for deriving the CO (6-5) flux upper limit). We compare this flux upper limit with the expected $435 \mu\text{m}$ continuum flux from an average infrared spectral energy distribution (SED) appropriate for the AGNs of X-ray luminosities comparable to that of NGC 5135: The intrinsic $2\text{-}10 \text{ keV}$ X-ray luminosity of NGC 5135 is $\sim 1.8 \times 10^{43} \text{ erg s}^{-1}$ (Singh et al. 2012). We therefore used the infrared AGN SED for $L_{2\text{-}10 \text{ keV}} > 10^{42.9} \text{ erg s}^{-1}$ in Mullaney et al. (2011) and anchored it at the $12 \mu\text{m}$ luminosity of NGC 5135 estimated from the X-ray and mid-IR correlation given in Asmus et al. (2015). This derived SED is shown in Fig. 6, along with two continuum flux upper limits (at 3σ) at 435 and $1,300 \mu\text{m}$ based on the ALMA observation. The latter continuum flux upper limit was estimated from an archival ALMA Band-6 observation (Project 2013.1.00243.S; PI: L. Colina). This plot suggests that the ALMA data points are consistent with what is expected from the typical infrared SED for AGNs like NGC 5135.

4.2. Properties of Molecular Gas Clumps

Several clumpy features are resolved in the CO (6-5) image shown in Fig. 1a. The resolved clump sizes of $\sim 100 \text{ pc}$ are comparable with or larger than the beam size. For other (U)LIRGS, such clumpy features are traced more commonly by low- J CO or isotopologues, owing to the difficulty in observing dense tracers. However, it is more appropriate to analyse the properties of compact clumpy structures as seen in Fig. 1a using denser gas tracers rather than the diffuse gas traced by low- J CO observation. Dense gas tracers, such as CS (2-1), HCN (1-0) and CO (6-5) usually trace embedded cloud clumps or cores within a more extended distribution of CO emission (Leroy et al. 2015; Sakamoto et al. 2011; Rosolowsky & Blitz 2005), and therefore are very useful for studying the dense, embedded star-forming structures within a much larger molecular region.

In Fig. 1a, the CO (6-5) emission peaks are resolved into separate clumps at $S/N = 4$, labelled as $a1$, $a2$, $a3$, $a4$, $a5$, b , c and d . For each clump, we list in Table 2 a number of parameters derived from the image in Fig. 1a for all the clumps except for the clump d . At the resolution of Fig. 1a, the clump d is detected only at $S/N =$

3 and appears to be quite diffuse. We therefore derived its parameters from the image in Fig. 3a, which has a coarser resolution of 112×112 pc.

The size of a clump is specified by its FWHM major and minor axes plus the major axis position angle (PA), which are respectively given in Columns (2) and (3) of Table 2. These were derived from a 2d Gaussian fit to the clump intensity map. For the blended clumps (*a4* and *a5*), we segmented the cloud into sub-clouds employing a variant of the CLUMPFIND algorithm (Williams et al. 1994). We divided the blended clumps by the half distance of two peaks and measure their parameters. We also calculated the effective clump radius R , following Solomon et al. (1987). After the deconvolution with the appropriate ALMA beam (using the CASA function “deconvolvefrombeam”), the radii range from 45 to 180 pc for the clumps (see Table 2, Column (4)).

We also extracted the 1d spectrum for each clump within an elliptical aperture with radii of (major and minor axes (FWHM)) as the oval areas marked in Fig. 1a. The resulting spectra are plotted for all the clumps in Fig. 7. Using the same elliptical aperture, we derived the integrated CO (6-5) flux from the clump intensity map and $435 \mu\text{m}$ continuum flux density from continuum map. The line central velocity, the line velocity width ΔV_{FWHM} , the integrated CO (6-5) flux and $435 \mu\text{m}$ continuum flux density given respectively in Columns (5), (6), (8) and (9) in Table 2. The resulting ΔV_{FWHM} ranges from 60 to 88 km s^{-1} .

We also estimated the Virial and molecular gas masses for each clump. Following Larson (1981); Heyer et al. (2009), the Virial mass (M_{vir}) is estimated as

$$M_{\text{vir}}/M_{\odot} = \frac{5 (\Delta V_{\text{FWHM}}/\text{km s}^{-1})^2 R/\text{pc}}{G}, \quad (1)$$

where R is simply the effective clump radius and ΔV_{FWHM} refers to the value of after deconvolution with channel width 13.5 km s^{-1} and a possible contribution of about 10 km s^{-1} from the disk rotation is further removed. (This correction amount was set to the mean velocity change over the size of one ALMA beam by examining the P-V plots of all the clumps. In the following, the ΔV_{FWHM} which we have used in Fig. 8 and 9 are those corrected ones.) The derived Virial masses, shown in Column (10) of Table 2, range from ~ 7 to $60 \times 10^7 M_{\odot}$.

We estimated the molecular gas mass of a clump, M_{mol} , using the $850 \mu\text{m}$ continuum flux density-based formula in Scoville et al. (2016) by converting the observed $435 \mu\text{m}$ flux density to that at $850 \mu\text{m}$ assuming a dust temperature of the 25 K:

$$L_{\nu_{850} \mu\text{m}} = 1.19 \times 10^{27} \times S_{\nu} / \text{Jy} \times \frac{(\nu_{850} \mu\text{m})^{3.8}}{\nu_{\text{obs}}(1+z)} \times \frac{(d_L/\text{Mpc})^2}{1+z} \times \frac{\Gamma_{\text{RJ}}(25, \nu_{850} \mu\text{m}, 0)}{\Gamma_{\text{RJ}}(25, \nu_{\text{obs}}, z)} / (\text{erg s}^{-1} \text{Hz}^{-1}) \quad (2)$$

and

$$\alpha_{\nu} = L_{\nu_{850} \mu\text{m}} / M_{\text{mol}} = 6.7 \pm 1.7 \times 10^{19} / (\text{erg s}^{-1} \text{Hz}^{-1} M_{\odot}^{-1}) \quad (3)$$

Where $\Gamma_{\text{RJ}}(T_d, \nu, z) = \frac{h\nu/kT_d}{e^{h\nu/kT_d} - 1}$ and the S_{ν} is the

dust emission flux density. As the $435 \mu\text{m}$ flux density shown in Table 2 is measured within FWHM (diameter), it should only account for about 58% of the total flux. Thus, we multiply the flux density by 1.731 to estimate the total flux. For the gas clumps in the nuclear region of NGC 5135, T_d could be warmer. In this case, the calculated M_{mol} would be overestimated by roughly a factor of $T_d/(25 \text{ K})$. The resulting M_{mol} , given in Column (11) of Table 2, ranges from ~ 1 to $10 \times 10^8 M_{\odot}$.

To check the molecular gas mass, we derived the molecular gas mass from the CO flux. We chose the conversion factor $\alpha_{\text{CO}} = 0.8 M_{\odot} (\text{K km s}^{-1} \text{pc}^2)^{-1}$ (Downes & Solomon 1998). The CO (6-5)/CO (1-0) is about 2 (this will be explained in Sec. 4.3.1). The molecular gas mass derived this way is consistent with the one derived from the dust continuum as shown in Column (12) of Table 2.

Table 2 shows that all clumps have $M_{\text{mol}} > M_{\text{vir}}$ except for the clumps *b* and *d*. The clumps in the former category (hereafter referred to as Category (i)) are likely to be self-gravitationally bound or even undergoing initial collapse. On the other hand, the clumps *b* and *d* in the other category (hereafter Category (ii)) would require external pressure to remain bound. Interestingly, the Category (ii) clumps are far away from on-going SF activity and also show significantly higher CO (6-5)-to-dust continuum flux ratios (cf. Table 2, Column (13)) than the clumps in Category (i).

We can also compare the clumps in NGC 5135 with the molecular gas clouds in other galaxies. Fig. 8 is a plot of the cloud (FWHM) velocity dispersion as a function of the cloud radius for the clumps in NGC 5135 as well as discrete clouds in the center of the Milky Way, nearby spiral galaxies, and two starburst galaxies NGC 253 and IC 5179. In comparison to the molecular clouds over the disks of nearby normal galaxies, the clouds in the Milky Way center observed by Oka et al. (2001) have a larger line width, but a smaller size. In contrast, the clouds in the starburst galaxy NGC 253 (Leroy et al. 2015) and the LIRG IC 5179 (Zhao et al. 2017) show both larger sizes and broader line widths than clouds in the Milky Way center, but generally following the lines of equal gas surface density for the case of Virialized clouds. The clouds in the nuclear region of NGC 5135 are characterized by still larger sizes and line widths.

Fig. 9 is a plot of the parameter, $\Delta V_{\text{FWHM}}^2/R$, as a function of molecular gas mass surface density Σ for the same data set as in Fig. 8. The thick diagonal line shows the locus of Virialized clouds. For bound clouds clearly lying above this line, the cloud velocity width is likely a manifestation of some external pressure. The dashed curves in Fig. 9, taken from Field et al. (2011), indicate the relationship between $\Delta V_{\text{FWHM}}^2/R$ and Σ for a varying external pressure. The Category (i) gas clumps in NGC 5135 lie around the line tracing the Virial equilibrium. In contrast, the two Category (ii) clumps are clearly located above the Virial equilibrium, and require external pressure of the order of $10^8 \text{ cm}^{-3} \text{K}$ in order to remain bound.

4.3. CO (6-5) Emission

4.3.1. CO (6-5) Emission to Continuum Ratio

On galaxy scale, the ratio of the CO (6-5) line luminosity, $L_{\text{CO}(6-5)}$, to L_{IR} varies only by up to 30% among lo-

cal LIRGs and shows little dependence on L_{IR} or the FIR color (Lu et al. 2014, 2017). This strongly requires that the energy sources for both the CO (6–5) and the dust emissions are ultimately tied to the same SF process. This narrows down the candidate heating mechanisms for the CO (6–5) emission to fewer choices, including photon heating in the photon dominant regions (PDRs) around young massive stars and SN-powered shock heating.

Our recent ALMA observation of nearby LIRGs show that, on scales of 100 pc or less, local peaks of the CO (6–5) emission do not always have corresponding peaks of the 435 μm dust continuum emission. Such examples include NGC 7130 (Zhao et al. 2016), IC 5179 (Zhao et al. 2017) and the case of NGC 5135 shown here. Under the assumption of a constant dust-to-gas abundance ratio, the spatial peaks of the two emissions should follow each other if both the dust and CO (6–5) emissions are related to the same photon heating. This finding therefore favors the SNe-powered shock gas heating scenario for the CO (6–5) emission. Here we investigate further this subject in the case of NGC 5135.

As shown in Column (13) of Table 2, the CO (6–5) flux to the 435 μm continuum flux density ratio, $R_{\text{CO}/\text{cont}}$, varies among the CO (6–5) clumps. Furthermore, while the Category (i) clumps satisfy $600 \lesssim R_{\text{CO}/\text{cont}} \lesssim 1800 \text{ km s}^{-1}$, the two Category (ii) clumps have $R_{\text{CO}/\text{cont}} > 4,000 \text{ km s}^{-1}$. It is evident in Table 2, the higher $R_{\text{CO}/\text{cont}}$ values associated with the Category (ii) clumps are mostly due to the unusually faint dust continuum emission at 435 μm . One can express

$$R_{\text{CO}/\text{cont}} \propto (f_{\text{CO}(6-5)}/f_{\text{CO}(1-0)}) (M_{\text{gas}}/M_{\text{dust}}) T_d^{-1}, \quad (4)$$

where we have assumed the CO (1–0) flux, $f_{\text{CO}(1-0)}$, scales with the molecular gas mass M_{gas} . This shows that a higher $R_{\text{CO}/\text{cont}}$ can stem from either a hotter CO gas or/and a cooler dust temperature. In the nuclear region of NGC 5135, the variation of T_d is limited to, perhaps, a factor of 3 (i.e., from 15 to 50 K) at most. The observed variation of $R_{\text{CO}/\text{dust}}$ is a factor of ~ 5 in Table 2, mainly between the two clump categories. A comparable variation is also seen in the case of IC 5179 (Zhao et al. 2017). Therefore, it requires a modest variation of a factor of 2 or so in $f_{\text{CO}(6-5)}/f_{\text{CO}(1-0)}$ in order to explain the observation. If the CO (6–5) emission is associated with SNe-shock heating, the ideal location for a higher $R_{\text{CO}/\text{cont}}$ ratio is where massive O star formation has ended while SNe activity is still strong, a scenario we discussed in the case of NGC 7130 (Zhao et al. 2016). A necessary condition for the validity of this scenario is that some dense gas can survive the massive star formation, which might be possible in dense and clumpy ISM.

4.3.2. CO (6–5) Emission and Current SF

In Fig. 10, the black contours of the integrated CO (6–5) line emission are overlaid on a ground-based 8.7 μm image (Díaz-Santos et al. 2008) on the left side, and on an *HST* Pa- α image (Alonso-Herrero et al. 2006) on the right. In both plots, we also show the low-resolution Chandra 0.4–8 keV broadband X-ray emission (Levenson et al. 2004) in red contours. This X-ray emission is mostly associated with a hot, ionized gas powered by SNRs (Levenson et al. 2004; Colina et al. 2012).

The 8.7 μm image is dominated by the mid-IR emission bands from the so-called Polycyclic Aromatic Hydrocarbons (PAHs). The Pa- α emission is caused by the ionizing UV radiation from massive O stars and is regarded as a reasonable tracer of the on-going SF activity (timescale ~ 10 Myr). The PAH emission traces SF of 10 times longer time scale (~ 100 Myr), as PAH molecules are mostly heated by non-ionizing B stars (Díaz-Santos et al. 2008). As shown in Fig. 10, the PAH and Pa- α emissions show similar surface brightness distributions. In contrast, the overall spatial morphology of the CO (6–5) emission appears to be different from that of either the PAH or the Pa- α emission. However, the Category (i) CO (6–5) clumps are all relatively close to local emission peaks of the PAH or Pa- α emission whereas the Category (ii) CO (6–5) clumps are significantly farther away from any bright PAH or Pa- α peak. Therefore, it is reasonable to expect a much weaker far-UV radiation intensity at the location of each Category (ii) clump. This naturally explains why the dust emission is unusually faint at each of the Category (ii) clumps.

4.4. Possible Heating Scenarios for CO (6–5) Emission

4.4.1. SN-powered Shock Heating Scenario

With an integral field spectrograph, Colina et al. (2012) measured the intensity and velocity fields of both the Br- γ and the [Fe II] 1.64 μm emission lines in the nuclear region of NGC 5135. While the Br- γ traces the current star formation, the [Fe II] line emission is regarded as a particularly good tracer of SNRs (Greenhouse et al. 1991). In Fig. 11, we show a plot of the [Fe II]-to-Br- γ line ratio versus the CO (6–5)-to-continuum flux density ratio for all the clumps listed in Table 2, except for clump *d*, which is located outside the field of view of the [Fe II] observation. We also indicated the typical [Fe II]-to-Br- γ line ratios for different astrophysical objects, taken from Falcón-Barroso et al. (2014). Note that the line ratio range shown for Seferts is largely irrelevant here as our molecular clouds are all located far away from the AGN.

A number of studies have attempted to identify the physical causes behind the observed variations of the [Fe II]-to-Br- γ line ratio (e.g., Alonso-Herrero et al. 1997; Moorwood & Oliva 1988; Mouri et al. 1990, 1993; Greenhouse et al. 1991; Rodríguez-Ardila et al. 2004, 2005; Ramos Almeida et al. 2006, 2009; Riffel et al. 2013; Falcón-Barroso et al. 2014). From these studies, two main conditions for an enhanced [Fe II] emission relative to a Hydrogen recombination line emission emerge: (a) Presence of shocked gas and (b) favorable environment for the gas-phase Fe to be abundant in the form of Fe⁺. Iron is normally depleted onto grains in the interstellar gas phase, so fast shocks, such as those associated with SNe, can cause grain destructions and therefore enrich gas-phase Fe abundance. Another important prerequisite for a strong [Fe II] line is an ionization field in favor of Fe⁺. Given the low ionization potential of Fe⁺ (16.2 eV), most of Fe is in higher ionization states in HII regions. In comparison, partially ionized gas in SNRs and Fe⁺ is believed to be abundant (Moorwood & Oliva 1988). The collisional excitation with electrons could therefore make the [Fe II] line much brighter in SNRs.

The [Fe II]-to-Br- γ line ratios for the Category (i) clumps in NGC 5135 are around 3, which is just out-

side the upper tip of the range for Galactic HII regions. These ratios are slightly higher than those seen in the nuclear star-forming regions in the Seyfert galaxy NGC 613 (Falcón-Barroso et al. 2014), suggesting some mild enhancement in the [Fe II] line emission for the gas clouds in NGC 5135. In comparison, this line ratio for the Category (ii) clump *b* equals 6.5, implying a factor of 2 further enhancement in the relative [Fe II] emission from the Category (i) clouds. It is not surprising for the observed line ratio of the Category (ii) cloud to be smaller than the typical values seen in Galactic SNRs because we are averaging over a much larger area than the typical size of Galactic SNRs and also because there is still low-surface brightness star forming activity near the cloud (see Fig. 10). The observed trend in Fig. 11 indicates that the same SNe shocks are likely to play a positive role in the observed variations in both [Fe II]/Br- γ and CO (6-5)/dust ratios.

Additional evidence in favor of the SNe-shock heating scenario for the CO (6-5) emission in NGC 5135 includes (a) the prevailing X-ray emission from the hot, ionized gas excited via SN shocks (Colina et al. 2012); and (b) that there is a very good velocity field correspondence between the CO (6-5) clumps and that of the underlying [Fe II] emission: the nominal CO (6-5) and [Fe II] line velocity offset varies around the mean of -142 km s^{-1} by only a few km s^{-1} among the clumps. (Note that the mean velocity field difference is likely a result of the different velocity reference frames adopted.) This velocity correspondence suggests that the warm CO gas and the shocked/ionized gas are reasonably well mixed with each other in space and velocity field. Another independent evidence in favor of the SNe-shock heating scenario is the global tight correlation between the IR dust emission and the mid-*J* CO line emission shown by Lu et al. (2017), which requires that the gas heating ultimately derives the energy from the same SF process. The SNe heating scenario would naturally fit this requirement.

4.4.2. Bar-Induced Shock Heating Scenario

Fig. 12 displays the integrated CO (6-5) line emission contours overlaid on the *HST* F606W ($0.606 \mu\text{m}$) image (Malkan et al. 1998) and *HST* F160W ($1.60 \mu\text{m}$) image (Alonso-Herrero et al. 2006), respectively. The *HST* images aligned with our CO (6-5) data by matching our adopted AGN position with the brightest point in each optical image. As already mentioned before, the CO (6-5) emission has a good spatial correspondence with the dust lanes that can be seen in the optical and near-IR continuum images here. These roughly symmetrical dust lanes are induced by the inner stellar bar, both of which are more visible in a larger UV/optical image such as the one shown by Mulchaey & Regan (1997). This correspondence between the CO (6-5) emission and the bar-induced dust lanes in NGC 5135 is similar to that observed in NGC 7130, another LIRG with a strong stellar bar (Zhao et al. 2016). Indeed NGC 5135 and NGC 7130 have many similarities: both are LIRGs with a strong circumnuclear star formation and a Seyfert 2 nucleus. Circumnuclear dust lanes have been found in many spiral galaxies, though strong 2-arm dust lanes are found only in barred galaxies such as NGC 5135 and NGC 7130 (Martini et al. 2003).

According to the model of Athanassoula (1992), the

2-arm dust lanes are associated with the shock fronts triggered by the presence of a bar in a rotating gas disk. Thus, bar-induced shocks could be possible in the nuclear region of NGC 5135. Inside the dust lanes, the gas (and dust) density is significantly enhanced, but SF is suppressed by strong shears (Athanassoula 1992). This seems to imply that the warm dense gas traced by CO (6-5) and the SF regions traced by Pa- α are not related to each other.

In order to account for the tight correlation between the CO (6-5) emission and the total dust emission on galaxy scale for LIRGs, one has to relate the CO (6-5) emitting gas to the SF activity in this scenario. It is still possible that the warm dense gas and the SF regions are related to each other, albeit their positions are slightly offset. It is known that some galaxies with weak stellar bars (therefore weaker shears in dust lanes) have SF in their dust lanes (Comte & Duquenooy 1982; Martini et al. 2003). Hypothetically, one can envisage the following scenario: First, SF does occur in clouds of dense gas formed in the post-shock gas down stream from the bar-induced shock front (the dust lane). Then these dense gas clouds will be rapidly consumed/destroyed by the SF and the associated feedback. In this scenario, under the assumption that the destruction time scale of the dense clouds is much shorter than the SF time scale associated with the Pa- α emission (a few Myrs), the spatial offset is the product of the SF time scale times the downstream velocity of the post-shock gas, which is a few 10 km s^{-1} (Athanassoula 1992). This indeed results in an estimate for the offset of $\lesssim 100 \text{ pc}$. It is worth noting that similar offset between HII regions and dust lanes associated with spiral arms in grand-design galaxies such as M 51 have been found in the literature, and Scoville et al. (2001) argued that it implies that the HII regions develop subsequent to the time of maximum concentration of the dust and molecular clouds.

However, it is unclear how this bar-induced shock heating scenario for the CO (6-5) emission can be made to explain the similar variation in the CO (6-5)-to-continuum flux ratio seen in IC 5179 (Zhao et al. 2017), which does not have a strong stellar bar.

5. SUMMARY

In this paper we present the results from our ALMA observations of the CO (6-5) line and its underlying dust continuum at $435 \mu\text{m}$ in the nuclear region of the nearby LIRG, Seyfert 2 galaxy NGC 5135, at a physical resolution of $48 \times 40 \text{ pc}$. Our main findings are:

(1) The central AGN is undetected in either the $435 \mu\text{m}$ dust continuum or CO (6-5) line emission if its line velocity width is no less than $\sim 40 \text{ km s}^{-1}$, resulting in an AGN contributes at most 1% of the integrated circumnuclear CO (6-5) flux seen in our ALMA observation. On the other hand, the non-detection in continuum emission may simply reflect the lack of sensitivity in our observation.

(2) The circum-nuclear CO (6-5) emission is resolved into gas clumps of radii of $45\text{-}180 \text{ pc}$ and line velocity widths of $60\text{-}88 \text{ km s}^{-1}$. While the clump sizes are only slightly larger than typical giant molecular clouds in nearby spiral galaxies, their velocity widths are significantly higher. They fall into two categories: (i) The 5 clumps that are near some current star formation activity

are likely to be in Virial equilibrium, and (ii) the other 2 clumps without clear current star formation activity nearby seem to be unbound unless there is significant external pressure.

(3) The clumps in Category (ii) have much higher CO (6–5) to dust continuum ratios than those in Category (i). Furthermore, the CO (6–5)-to-continuum ratios show an increasing trend with the [Fe II]-to-Br- γ ratios, which we interpret as evidence for supernova-driven shocked gas providing a significant contribution to the CO (6–5) emission.

(4) The clumps are distributed along the symmetric optical dust lanes associated with the stellar bar at the center of the galaxy. Like NGC 7130, another barred Seyfert galaxy, the gas concentrations could be a result of the bar-induced instability and is subject to bar-induced shock heating.

ACKNOWLEDGMENTS

We thank an anonymous referee for a number of very constructive comments. We thank Drs. Cheng Cheng,

Luis Colina, Adam Leroy, Claudio Ricci, and Chentao Yang for their insightful comments and/or useful communications during the preparation of the manuscript. This paper makes use of the following ALMA data: ADS/JAO.ALMA#2013.1.00524.S. ALMA is a partnership of ESO (representing its member states), NSF (USA), and NINS (Japan), together with NRC (Canada) and NSC and ASIAA (Taiwan), in cooperation with the Republic of Chile. The Joint ALMA Observatory is operated by ESO, AUI/NRAO, and NAOJ. This work is supported in part by the National Key R&D Program of China grant #2017YFA0402704, the NSFC grant #11673028 and #11673057, and by the Chinese Academy of Sciences (CAS), through a grant to the CAS South America Center for Astronomy (CAS-SACA) in Santiago, Chile. C.C. acknowledges support by NSFC grant No.11503013. Y.G. acknowledges support by NSFC grants No.11173059, 11390373, and 11420101002. H.W. acknowledges support by NSFC grant No.11733006. V.K. acknowledges support from the FONDECYT grant No.3160117. T.D.-S. acknowledges support from ALMA-CONICYT project 31130005 and FONDECYT regular project 1151239.

REFERENCES

- Aalto, S., Muller, S., Costagliola, F., et al. 2017, *A&A*, 608, A22
 Alonso-Herrero, A., Rieke, G. H., Rieke, M. J., et al. 2006, *ApJ*, 650, 835
 Alonso-Herrero, A., Rieke, M. J., Rieke, G. H., & Ruiz, M. 1997, *ApJ*, 482, 747
 Armus, L., Mazzarella, J. M., Evans, A. S., et al. 2009, *PASP*, 121, 559
 Asmus, D., Gandhi, P., Hönic, S. F., Smette, A., & Duschl, W. J. 2015, *MNRAS*, 454, 766
 Athanassoula, E. 1992, *MNRAS*, 259, 345
 Bedregal, A. G., Colina, L., Alonso-Herrero, A., & Arribas, S. 2009, *ApJ*, 698, 1852
 Bradford, C. M., Nikola, T., Stacey, G. J., et al. 2003, *ApJ*, 586, 891
 Bryant, P. M., & Scoville, N. Z. 1999, *AJ*, 117, 2632
 Caputi, K. I., Lagache, G., Yan, L., et al. 2007, *ApJ*, 660, 97
 Colina, L., Pereira-Santaella, M., Alonso-Herrero, A., Bedregal, A. G., & Arribas, S. 2012, *ApJ*, 749, 116
 Comte, G., & Duquenois, A. 1982, *A&A*, 114, 7
 Díaz-Santos, T., Alonso-Herrero, A., Colina, L., et al. 2008, *ApJ*, 685, 211
 Díaz-Santos, T., Armus, L., Charmandaris, V., et al. 2017, *ApJ*, 846, 32
 Downes, D., & Solomon, P. M. 1998, *ApJ*, 507, 615
 Espada, D., Matsushita, S., Miura, R. E., et al. 2017, *ApJ*, 843, 136
 Evans, A. S., Mazzarella, J. M., Surace, J. A., & Sanders, D. B. 2002, *ApJ*, 580, 749
 Falcón-Barroso, J., Ramos Almeida, C., Böker, T., et al. 2014, *MNRAS*, 438, 329
 Field, G. B., Blackman, E. G., & Keto, E. R. 2011, *MNRAS*, 416, 710
 Fukazawa, Y., Hiragi, K., Mizuno, M., et al. 2011, *ApJ*, 727, 19
 Gao, Y., & Solomon, P. M. 1999, *ApJ*, 512, L99
 García-Burillo, S., Combes, F., Usero, A., et al. 2014, *A&A*, 567, A125
 García-Burillo, S., Combes, F., Ramos Almeida, C., et al. 2016, *ApJ*, 823, L12
 González Delgado, R. M., Heckman, T., Leitherer, C., et al. 1998, *ApJ*, 505, 174
 Greenhouse, M. A., Woodward, C. E., Thronson, Jr., H. A., et al. 1991, *ApJ*, 383, 164
 Griffin, M. J., Abergel, A., Abreu, A., et al. 2010, *A&A*, 518, L3
 Gruppioni, C., Pozzi, F., Rodighiero, G., et al. 2013, *MNRAS*, 432, 23
 Heyer, M., Krawczyk, C., Duval, J., & Jackson, J. M. 2009, *ApJ*, 699, 1092
 Kamenetzky, J., Glenn, J., Rangwala, N., et al. 2012, *ApJ*, 753, 70
 Kawamura, A., Mizuno, Y., Minamidani, T., et al. 2009, *ApJS*, 184, 1
 Larson, R. B. 1981, *MNRAS*, 194, 809
 Le Floch, E., Papovich, C., Dole, H., et al. 2005, *ApJ*, 632, 169
 Leroy, A. K., Bolatto, A. D., Ostriker, E. C., et al. 2015, *ApJ*, 801, 25
 Levenson, N. A., Weaver, K. A., Heckman, T. M., Awaki, H., & Terashima, Y. 2004, *ApJ*, 602, 135
 Lu, N., Zhao, Y., Xu, C. K., et al. 2014, *ApJ*, 787, L23
 Lu, N., Zhao, Y., Díaz-Santos, T., et al. 2017, *ApJS*, 230, 1
 Magnelli, B., Elbaz, D., Chary, R. R., et al. 2009, *A&A*, 496, 57
 —. 2011, *A&A*, 528, A35
 Malkan, M. A., Gorjian, V., & Tam, R. 1998, *ApJS*, 117, 25
 Martini, P., Regan, M. W., Mulchaey, J. S., & Pogge, R. W. 2003, *ApJS*, 146, 353
 McMullin, J. P., Waters, B., Schiebel, D., Young, W., & Golap, K. 2007, in *Astronomical Society of the Pacific Conference Series*, Vol. 376, *Astronomical Data Analysis Software and Systems XVI*, ed. R. A. Shaw, F. Hill, & D. J. Bell, 127
 Meijerink, R., Kristensen, L. E., Weiß, A., et al. 2013, *ApJ*, 762, L16
 Moorwood, A. F. M., & Oliva, E. 1988, *A&A*, 203, 278
 Mouri, H., Kawara, K., & Taniguchi, Y. 1993, *ApJ*, 406, 52
 Mouri, H., Nishida, M., Taniguchi, Y., & Kawara, K. 1990, *ApJ*, 360, 55
 Muñoz Marín, V. M., González Delgado, R. M., Schmitt, H. R., et al. 2007, *AJ*, 134, 648
 Mulchaey, J. S., & Regan, M. W. 1997, *ApJ*, 482, L135
 Mullaney, J. R., Alexander, D. M., Goulding, A. D., & Hickox, R. C. 2011, *MNRAS*, 414, 1082
 Nikola, T., Stacey, G. J., Brisbin, D., et al. 2011, *ApJ*, 742, 88
 Oka, T., Hasegawa, T., Sato, F., et al. 2001, *ApJ*, 562, 348
 Pellegrini, E. W., Smith, J. D., Wolfire, M. G., et al. 2013, *ApJ*, 779, L19
 Phillips, M. M., Charles, P. A., & Baldwin, J. A. 1983, *ApJ*, 266, 485
 Pilbratt, G. L., Riedinger, J. R., Passvogel, T., et al. 2010, *A&A*, 518, L1
 Ramos Almeida, C., Pérez García, A. M., & Acosta-Pulido, J. A. 2009, *ApJ*, 694, 1379
 Ramos Almeida, C., Pérez García, A. M., Acosta-Pulido, J. A., et al. 2006, *ApJ*, 645, 148

- Rangwala, N., Maloney, P. R., Wilson, C. D., et al. 2015, *ApJ*, 806, 17
- Rangwala, N., Maloney, P. R., Glenn, J., et al. 2011, *ApJ*, 743, 94
- Riffel, R., Rodríguez-Ardila, A., Aleman, I., et al. 2013, *MNRAS*, 430, 2002
- Rigopoulou, D., Hurley, P. D., Swinyard, B. M., et al. 2013, *MNRAS*, 434, 2051
- Rodríguez-Ardila, A., Pastoriza, M. G., Viegas, S., Sigut, T. A. A., & Pradhan, A. K. 2004, *A&A*, 425, 457
- Rodríguez-Ardila, A., Riffel, R., & Pastoriza, M. G. 2005, *MNRAS*, 364, 1041
- Rosenberg, M. J. F., Meijerink, R., Israel, F. P., et al. 2014, *A&A*, 568, A90
- Rosolowsky, E., & Blitz, L. 2005, *ApJ*, 623, 826
- Sakamoto, K., Mao, R.-Q., Matsushita, S., et al. 2011, *ApJ*, 735, 19
- Sanders, D. B., & Mirafbel, I. F. 1996, *ARA&A*, 34, 749
- Sanders, D. B., Scoville, N. Z., & Soifer, B. T. 1991, *ApJ*, 370, 158
- Sanders, D. B., Scoville, N. Z., Young, J. S., et al. 1986, *ApJ*, 305, L45
- Scoville, N., Sheth, K., Aussel, H., et al. 2016, *ApJ*, 820, 83
- Scoville, N. Z., Polletta, M., Ewald, S., et al. 2001, *AJ*, 122, 3017
- Singh, V., Risaliti, G., Braito, V., & Shastri, P. 2012, *MNRAS*, 419, 2089
- Sliwa, K., Wilson, C. D., Aalto, S., & Privon, G. C. 2017, *ApJ*, 840, L11
- Soifer, B. T., Sanders, D. B., Madore, B. F., et al. 1987, *ApJ*, 320, 238
- Solomon, P. M., Downes, D., Radford, S. J. E., & Barrett, J. W. 1997, *ApJ*, 478, 144
- Solomon, P. M., Rivolo, A. R., Barrett, J., & Yahil, A. 1987, *ApJ*, 319, 730
- Solomon, P. M., & Sage, L. J. 1988, *ApJ*, 334, 613
- Spaans, M., & Meijerink, R. 2008, *ApJ*, 678, L5
- Spinoglio, L., Pereira-Santaella, M., Busquet, G., et al. 2012, *ApJ*, 758, 108
- Turner, T. J., George, I. M., Nandra, K., & Mushotzky, R. F. 1997, *ApJS*, 113, 23
- Ulvestad, J. S., & Wilson, A. S. 1989, *ApJ*, 343, 659
- Wang, J. L., Xia, X. Y., Mao, S., et al. 2006, *ApJ*, 649, 722
- Williams, J. P., de Geus, E. J., & Blitz, L. 1994, *ApJ*, 428, 693
- Wilson, C. D., Rangwala, N., Glenn, J., et al. 2014, *ApJ*, 789, L36
- Wootten, A., & Thompson, A. R. 2009, *IEEE Proceedings*, 97, 1463
- Xu, C. K., Cao, C., Lu, N., et al. 2014, *ApJ*, 787, 48
- . 2015, *ApJ*, 799, 11
- Zhao, Y., Lu, N., Xu, C. K., et al. 2016, *ApJ*, 820, 118
- Zhao, Y., Lu, N., Díaz-Santos, T., et al. 2017, *ApJ*, 845, 58

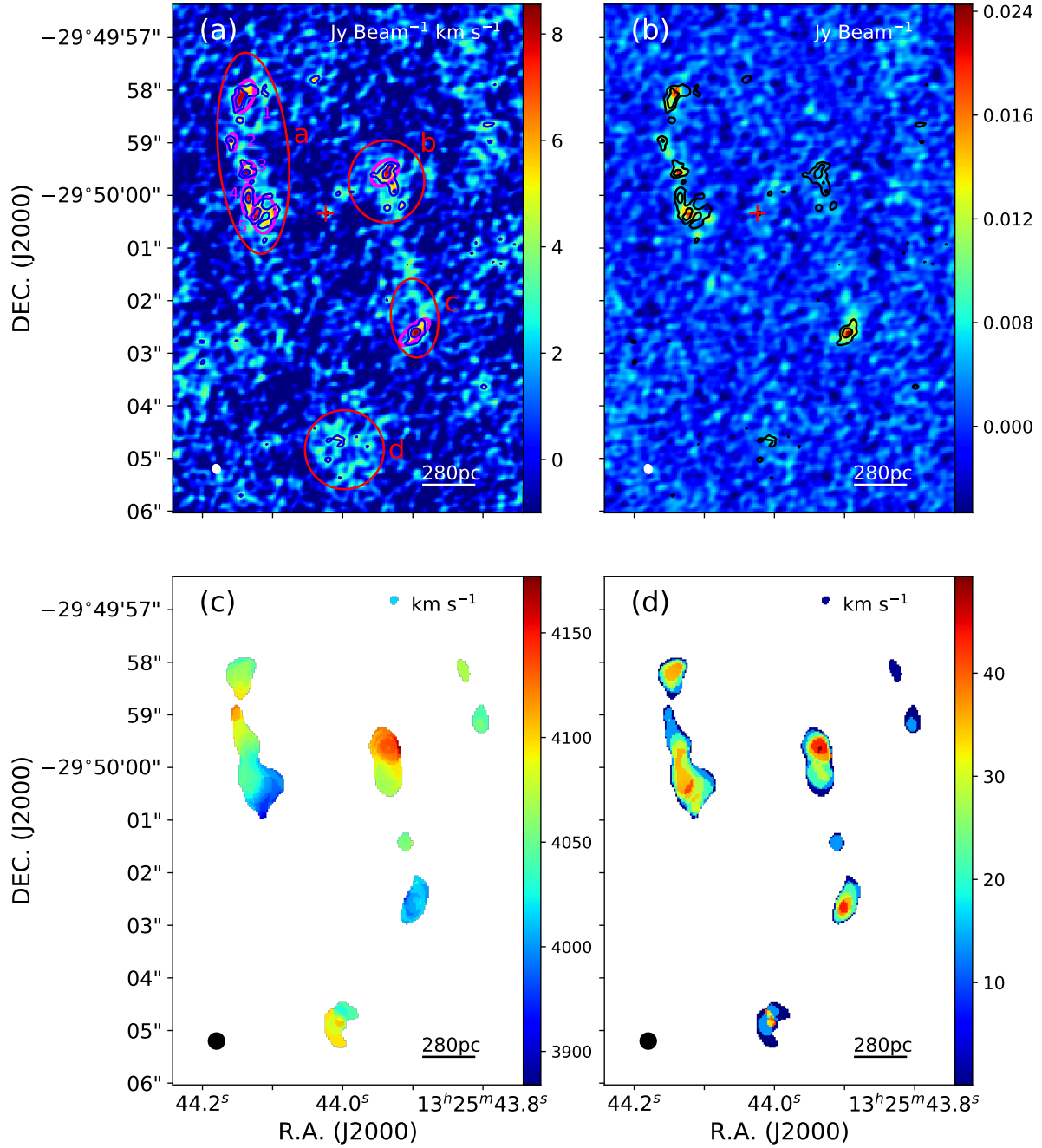


FIG. 1.— Panels (a) and (b): Contours of the frequency-integrated CO (6-5) intensity overlaid on the images of the same integrated CO (6-5) intensity in (a) and the $435 \mu\text{m}$ dust continuum emission in (b). Panels (c) and (d) are respectively the line velocity field (moment 1) and the velocity dispersion (moment 2) maps of the CO (6-5) line emission obtained from the uv-taper image. The images in (c) and (d) are generated by using only those spaxels above $4\text{-}\sigma_{ch}$, where σ_{ch} is the r.m.s noise per frequency channel ($\sigma_{ch} = 40 \text{ mJy beam}^{-1}$ for uv-taper image). The contours in panels (a) and (b) are shown at $[3,5] \times \sigma$ (where the noise $\sigma = 1.2 \text{ Jy beam}^{-1} \text{ kms}^{-1}$). The unit of the color bar in each panel is given near the upper-right color. The filled ellipse in white near the lower-left corner in (a) or (b) is the ALMA beam. The large ellipses in red in (a) mark the regions for spectrum and flux extractions given in Table 2. The red plus sign marks the AGN position adopted. The figures are before the primary beam correction integrated over the barycentric velocities from 3,971 to 4,157 km s^{-1} .

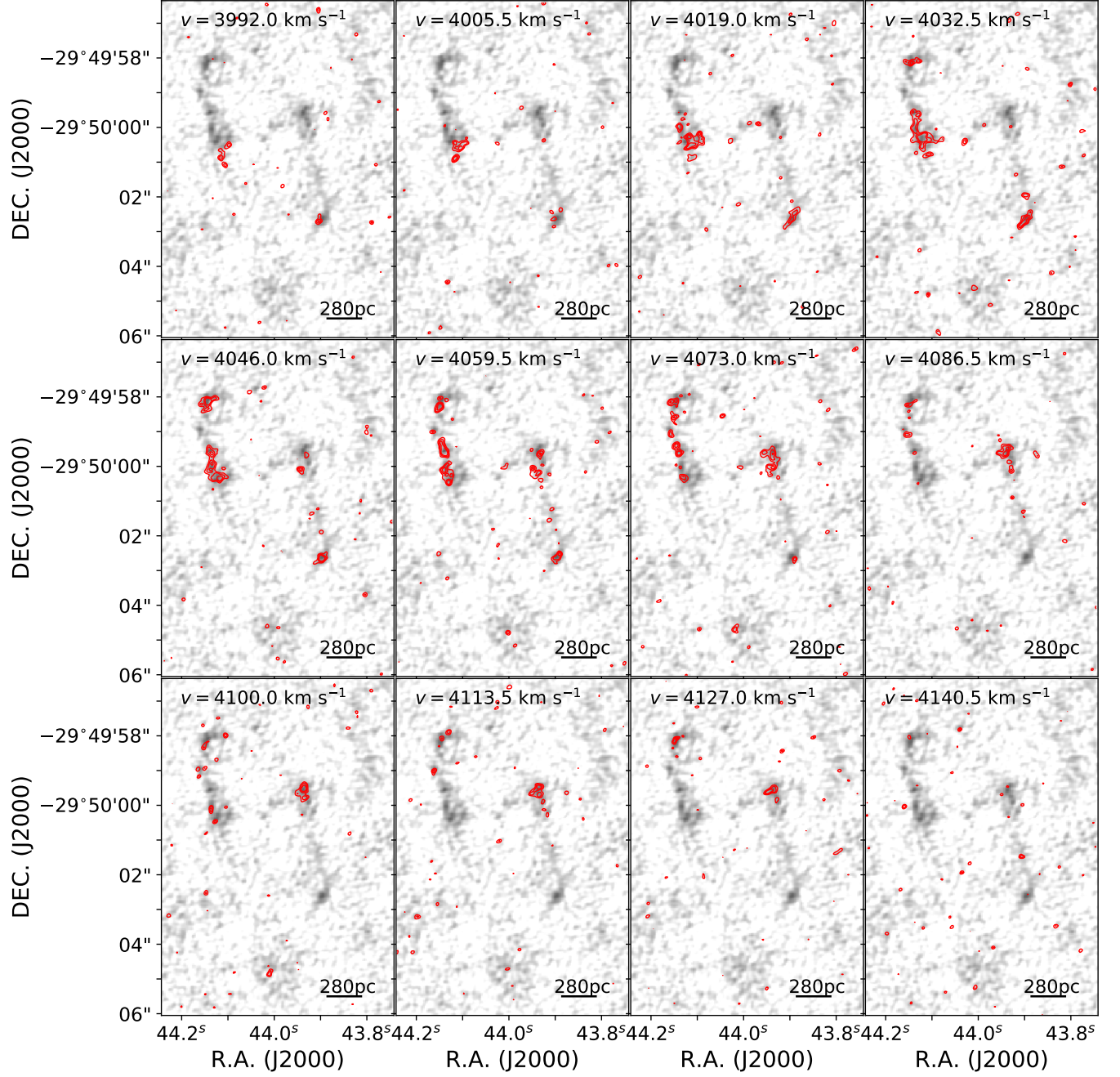


FIG. 2.— Channel maps of the CO (6-5) line emission (in contours), each overlaid on the image of the total, frequency-integrated CO (6-5) emission (e.g., from Fig. 1a). The channel interval is 13.5 km s^{-1} , with the channel central (barycentric) velocity shown in each channel map.

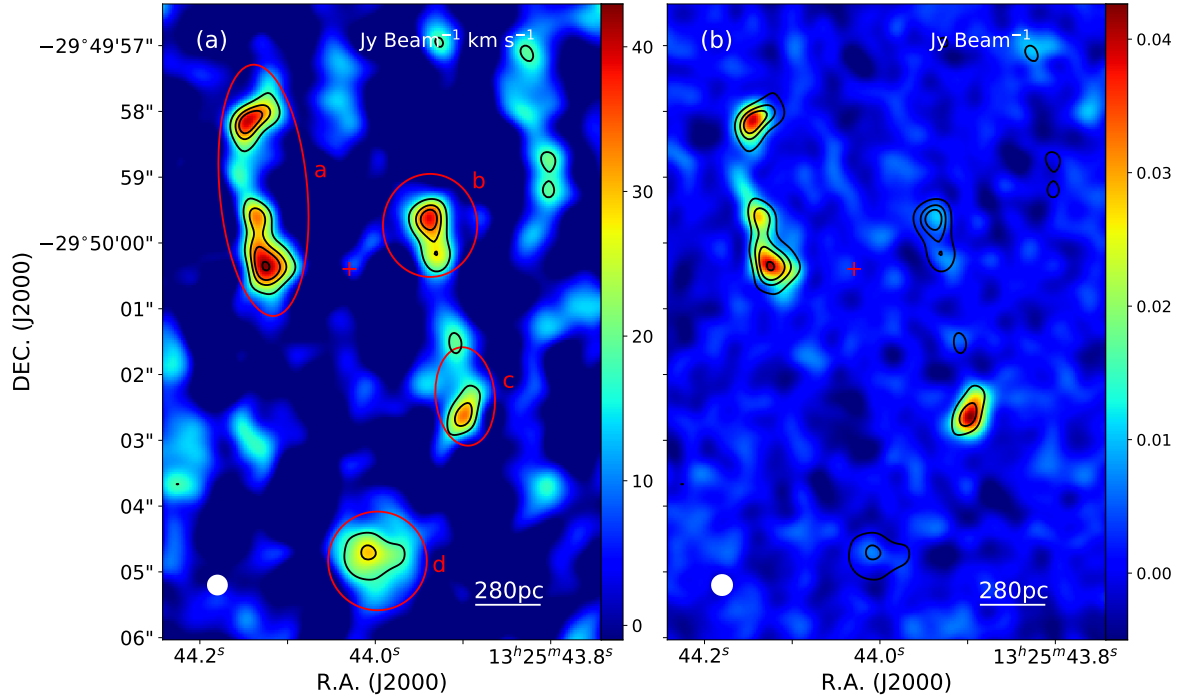


FIG. 3.— Same as the panels (a) and (b) in Fig. 1, respectively, but using the CO (6-5) and continuum data at a larger effective beam. The contour levels are $[3, 4, 5, 6] \times \sigma$ ($\sigma = 8 \text{ Jy beam}^{-1} \text{ km s}^{-1}$, with the beam size of $0.4'' \times 0.4''$ here as shown by the filled ellipse in white in each panel).

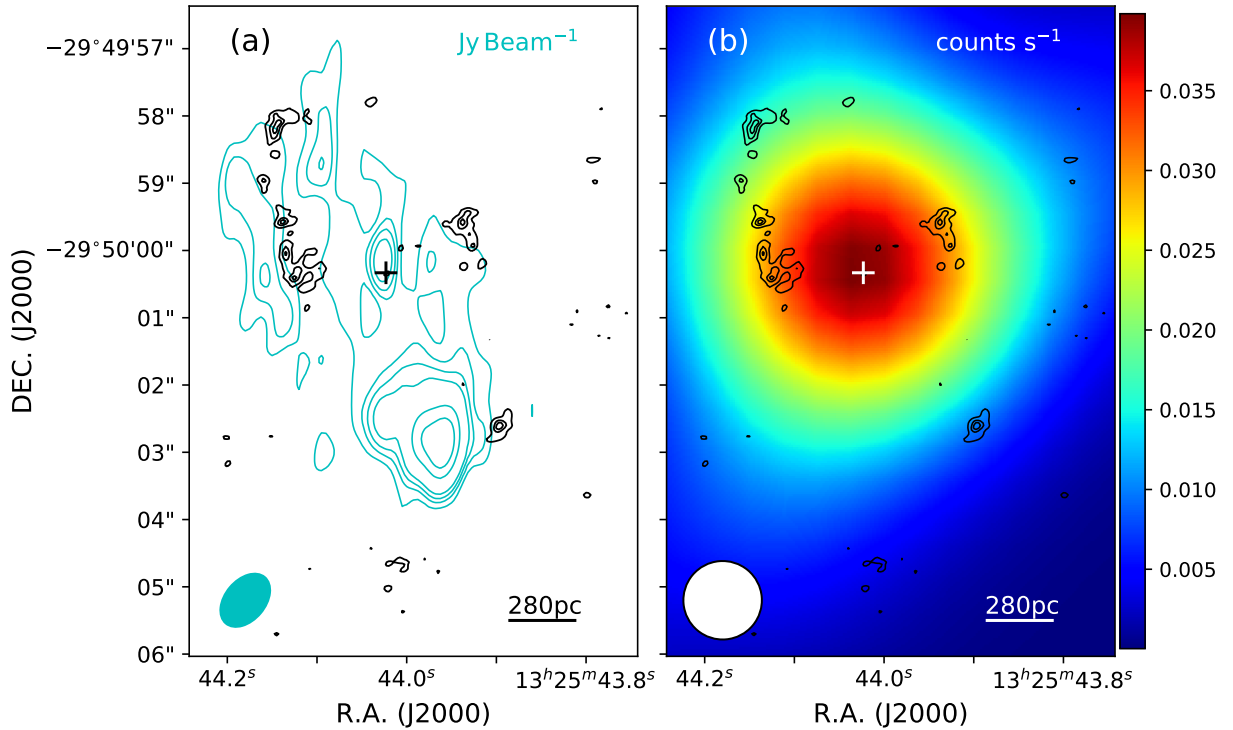


FIG. 4.— Black contours of the integrated CO (6-5) line emission overlaid on (a) an VLA radio cyan contours at 6cm (the cyan contour levels are $[3, 5, 7, 10, 30, 50] \times \sigma$ ($\sigma = 1.2 \times 10^{-4} \text{ Jy beam}^{-1}$) and (b) a Chandra 4-8 keV X-ray image. The black contour level are $[3, 5, 6] \times \sigma$ ($\sigma = 1.2 \text{ Jy beam}^{-1} \text{ km s}^{-1}$). The white plus sign in each panel presents the adopted AGN location.

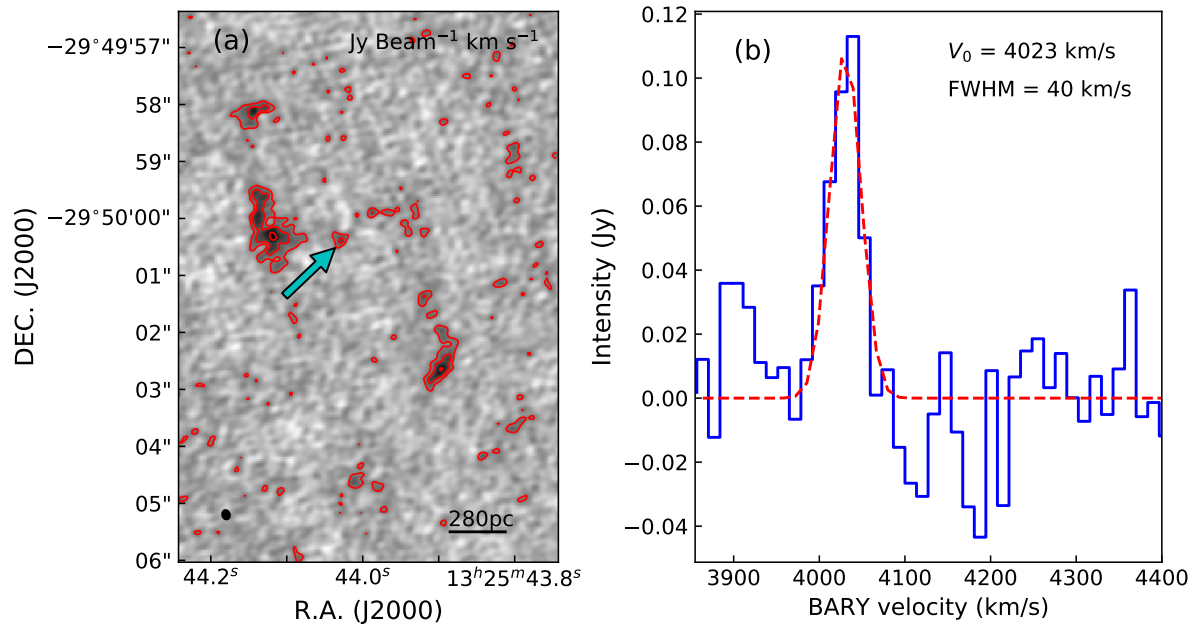


FIG. 5.— (a) Contours of the integrated CO (6-5) from 4019 to 4032 km/s on the image of the same integrated CO (6-5) intensity. The cyan arrow points to the central AGN. The contour levels are $[3, 5, 8] \times \sigma$ ($\sigma = 0.5 \text{ Jy beam}^{-1} \text{ km s}^{-1}$). And (b) the CO (6-5) spectrum at the central AGN. The central velocity (V_0) and FWHM of a Gaussian fit are given in the plot.

TABLE 1
BASIC PROPERTIES OF NGC 5135 AND ALMA OBSERVATION LOG

Basic Properties							
Name	R.A. (J2000) (hh:mm:ss)	Dec. (J2000) (dd:mm:ss)	Dist. Mpc	cz kms^{-1}	Morph	Spectral Type	$\log L_{\text{IR}}$ L_{\odot}
(1)	(2)	(3)	(4)	(5)	(6)	(7)	(8)
NGC 5135	13:25:43.99	-29:50:01.06	59	4105	SB (s)ab	Sy 2	11.33
ALMA observation log							
SB	Date (yyyy/mm/dd)	Time (UTC)	Configuration	N_{ant}	l_{max} (m)	t_{int} (seconds)	T_{sys} (K)
(1)	(2)	(3)	(4)	(5)	(6)	(7)	(8)
Xa216e2_Xcb0	2015/06/02-2015/06/03	23:58:10-00:51:44	C34-5	39	885.6	21.03	935 - 839

NOTE. — In the upper table section on galaxy basic properties: Col. 1: source name; Cols. 2 and 3: right ascension and declination; Col. 4: distance; Col. 5: heliocentric velocity; Col. 6: galaxy optical morphology; Col. 7: Nuclear activity classification; Col. 8: the total infrared luminosity (8-1000 μm). In the lower table section on ALMA observation log: Col. 1: schedule-block number; Cols. 2 and 3: observational date and time; Col. 4: observational configuration; Col. 5: number of usable 12-m antennae (i.e., un-flagged); Col. 6: maximum baseline length; Col. 7: on-source integration time; Col. 8: median system temperature.

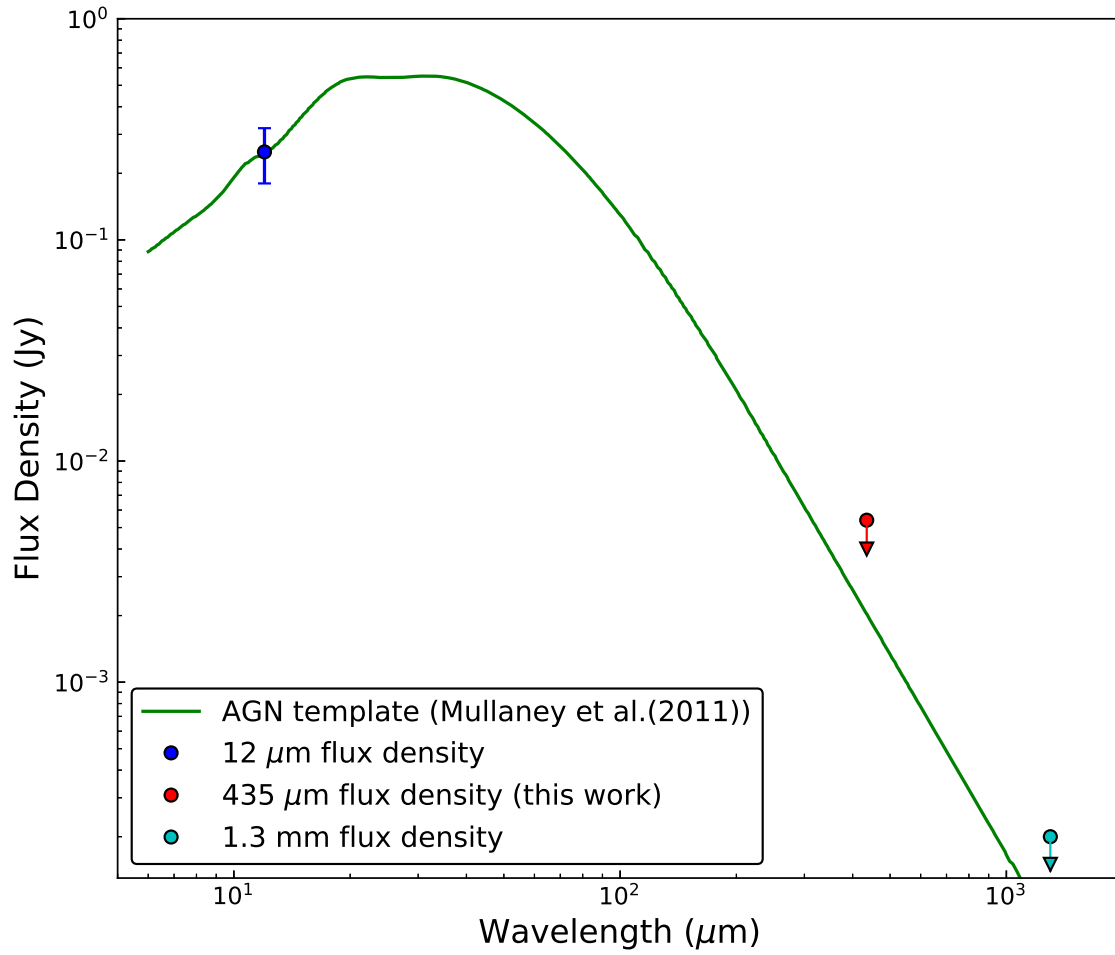


FIG. 6.— Plot of the empirical infrared spectrum (the green curve) of the AGN in NGC 5135, which is based the observed X-ray luminosity and anchored at the $12 \mu\text{m}$ flux density measurement (the filled circle in blue). Also shown are two ALMA flux upper limits at $435 \mu\text{m}$ and 1.3 mm , respectively (see the text).

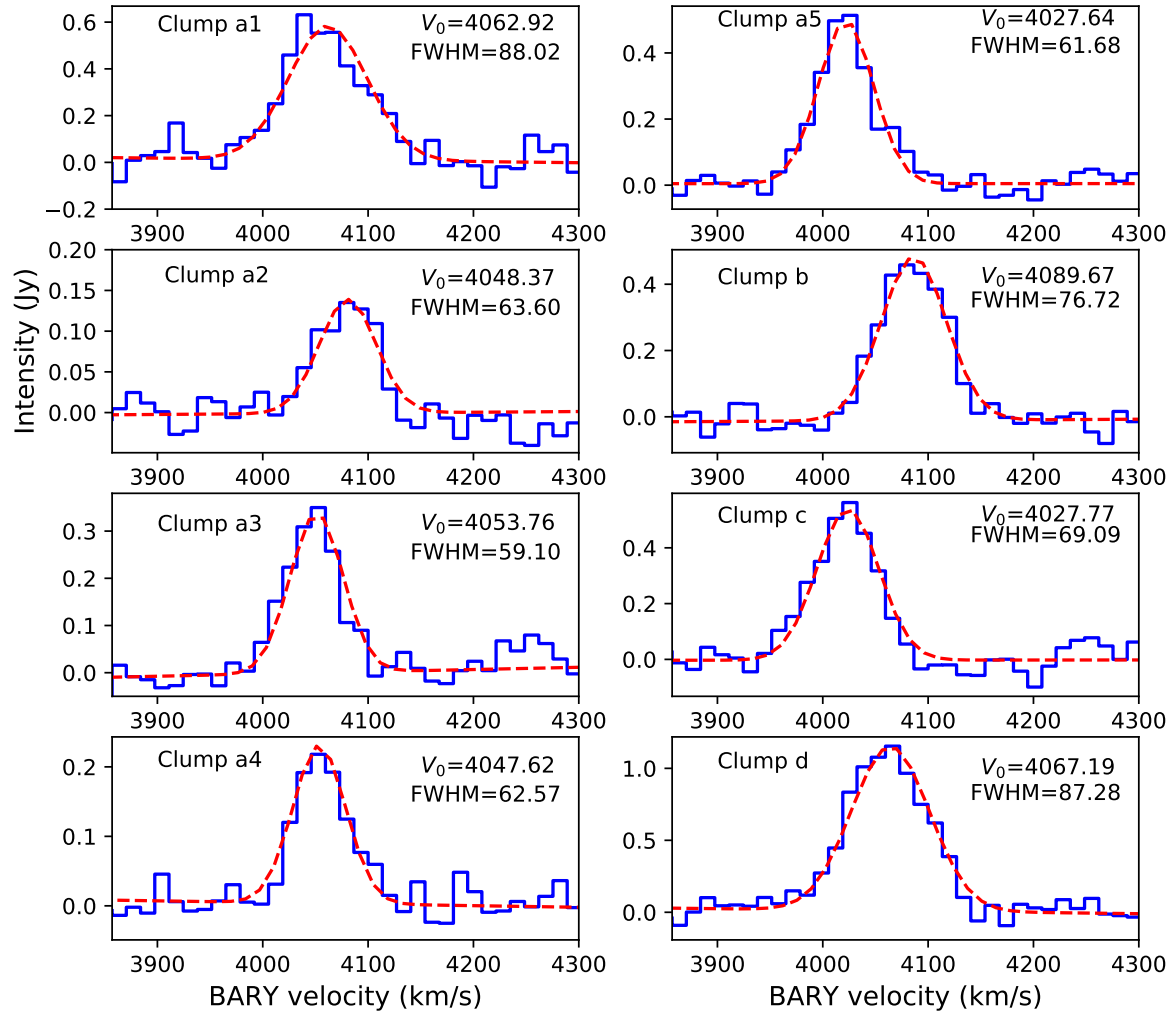


FIG. 7.— Spatially integrated CO (6-5) line profile of various clumps (a1, a2, a3, a4, a5, b, c, d). The central velocity (V_0) and FWHM of a Gaussian fit are given in each plot.

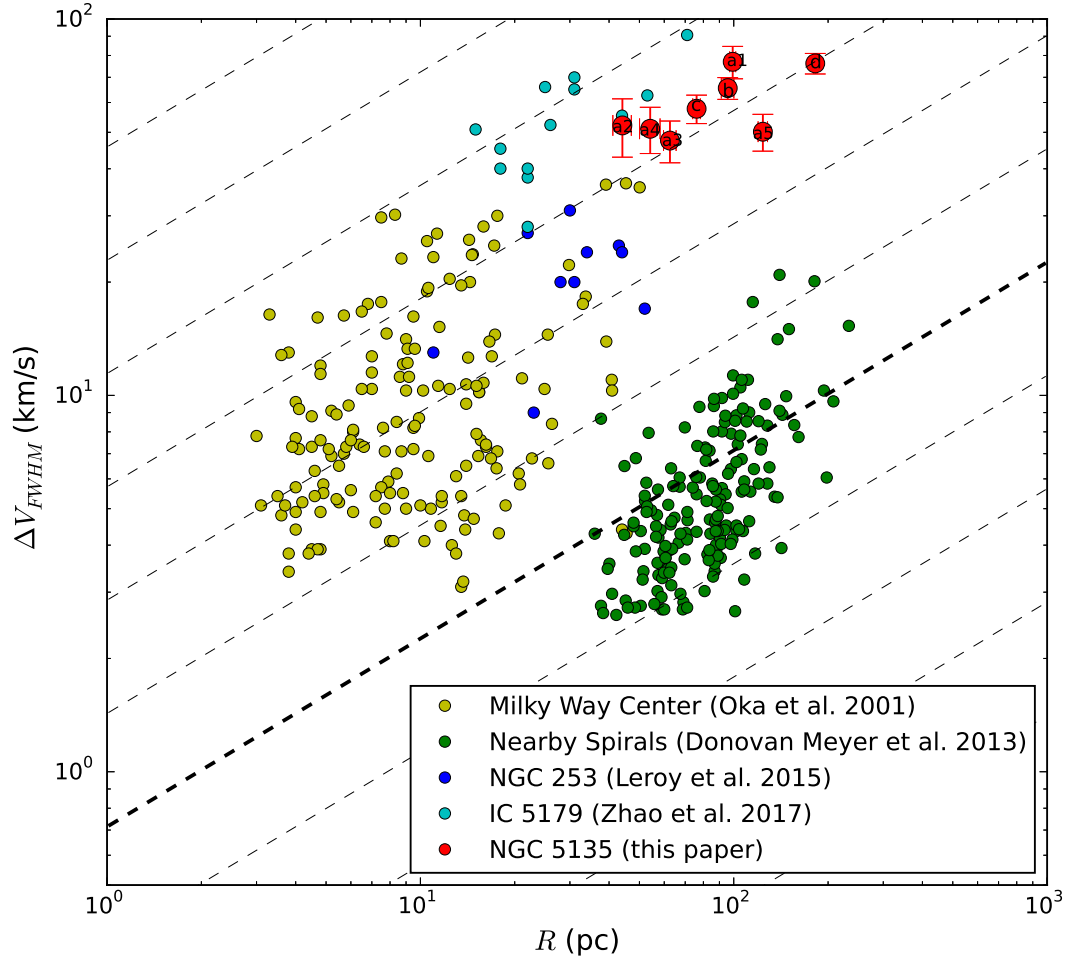


FIG. 8.— Plot of the CO (6-5) line width, ΔV_{FWHM} , as a function of the cloud radius R for a sample of giant molecular clouds and gas complexes in the Milky Way and various local galaxies, adopted from Leroy et al. (2015). As a comparison, our NGC 5135 clumps are added (i.e., large filled circles labeled by the clump number). The light dashed lines follow $\Delta V_{\text{FWHM}} \propto R^{0.5}$, the relation expected for Virialized clouds with a fixed surface density Σ , spaced by a factor of 2 vertically. The thick dashed line is for $\Sigma \approx 285 \text{ M}_{\odot} \text{ pc}^{-2}$.

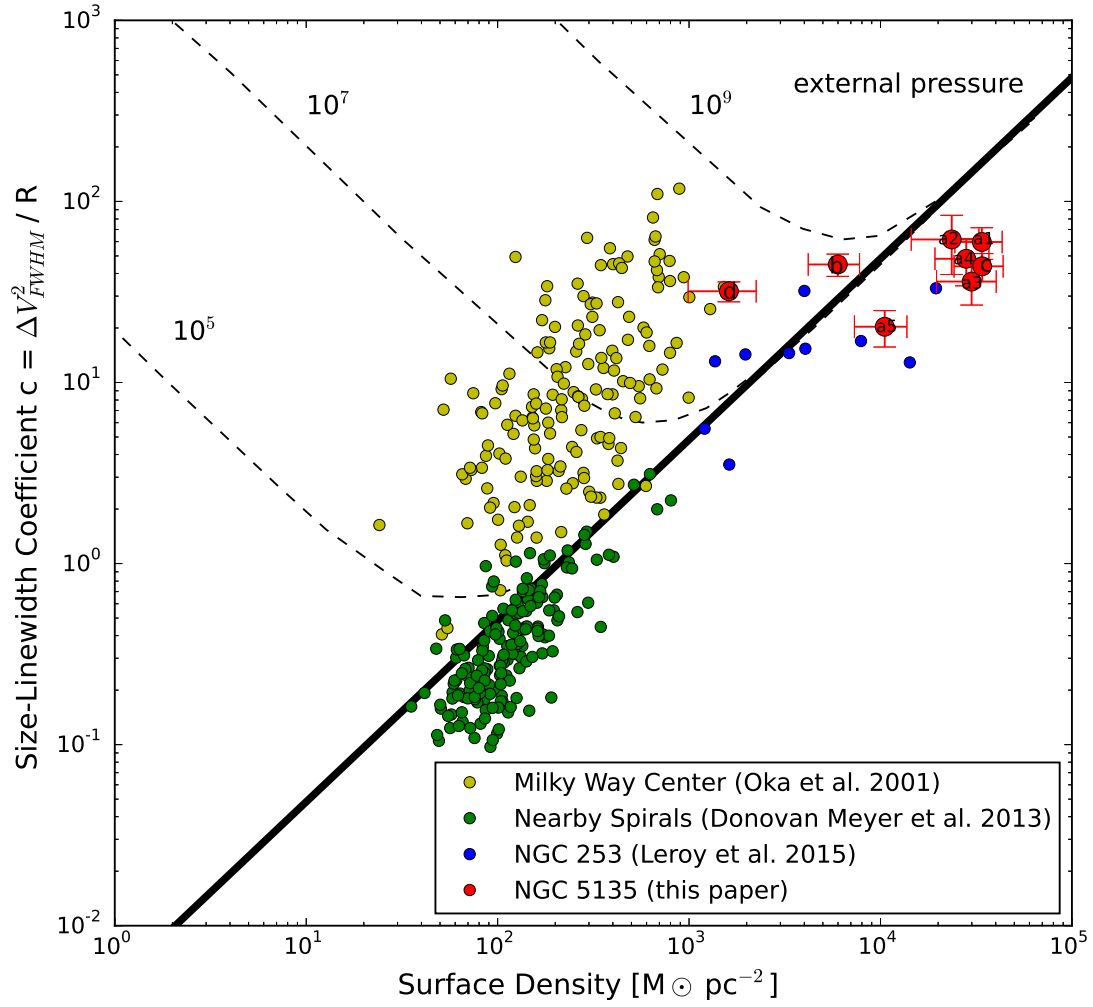


FIG. 9.— Plot of the cloud radius-line width coefficient, $\Delta V_{FWHM}^2/R$, as a function of the gas surface density Σ , also adopted from Leroy et al. (2015), for the same data set as in Fig. 7. The gas clouds that are in Virial equilibrium (i.e., $M_{\text{mol}} = M_{\text{vir}}$) follow the thick line. Bound clouds with $M_{\text{mol}} < M_{\text{vir}}$ follow one of the thin curves representing various external pressures as labelled in terms of P/k_B (in units of $\text{cm}^{-3} \text{ K}$).

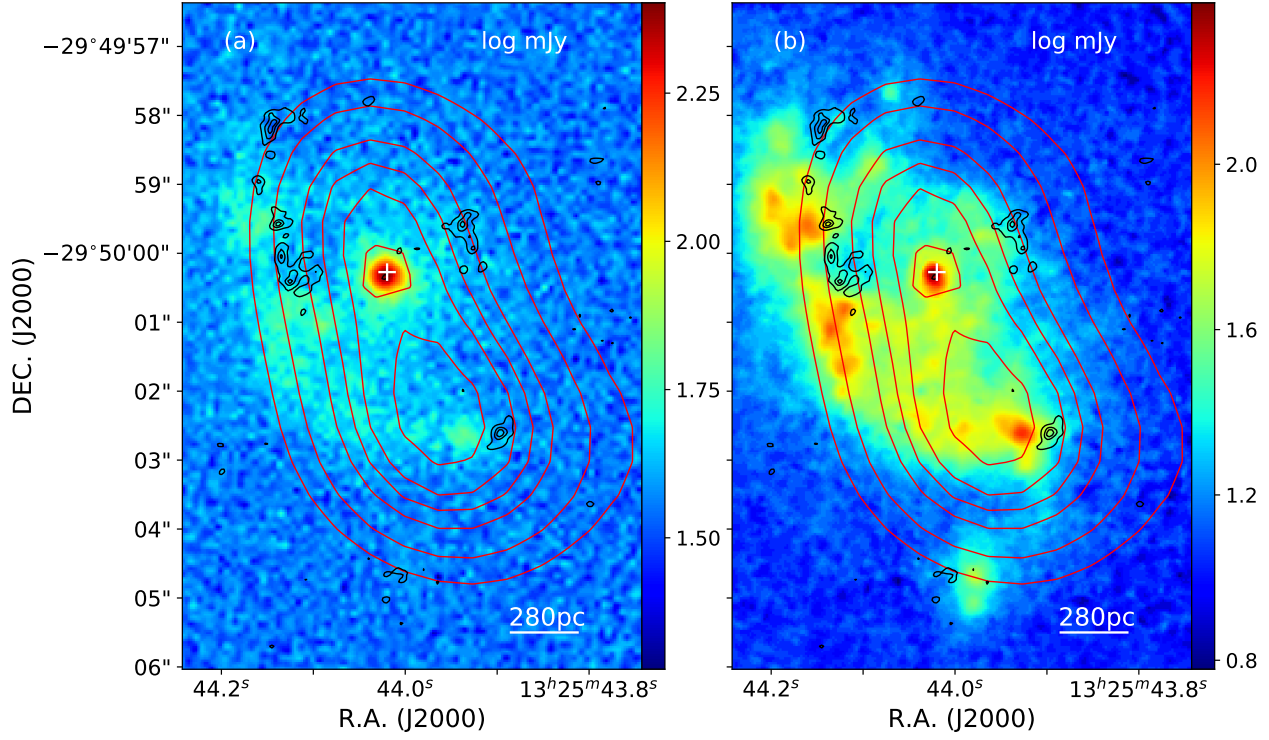


FIG. 10.— Integrated CO (6-5) line emission contours, at $[3, 5, 6] \times \sigma$ (where $\sigma = 1.2 \text{ Jy beam}^{-1} \text{ km s}^{-1}$), overlaid on (a) a $8.7 \mu\text{m}$ image dominated by the PAH emission (in log scale) and (b) an image of the Pa- α line emission (in log scale). The red contours in each panel stand for the X-ray intensity of NGC 5135 (with the contours at 5, 20, 30, 40, 70, 150, 260 counts), obtained in the Chandra 0.4-8 keV band by Levenson et al. (2004). The white plus sign in each panel marks the adopted AGN location.

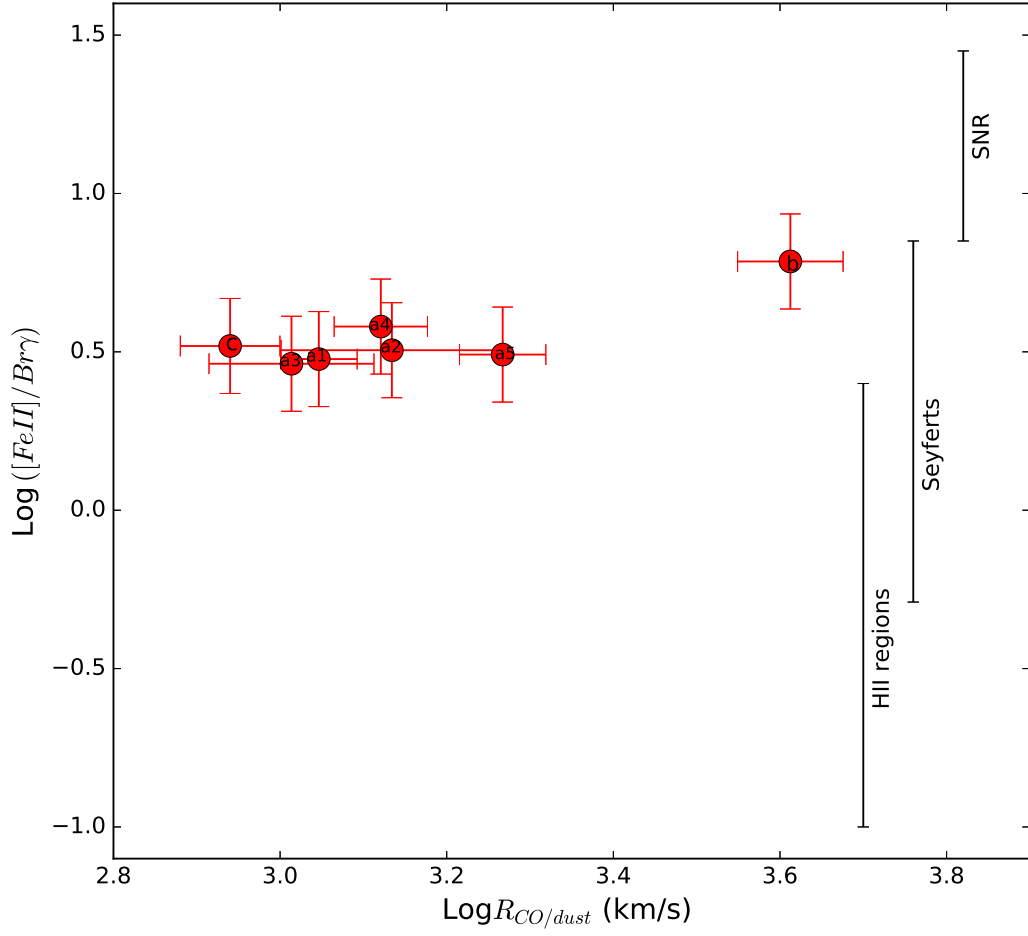


FIG. 11.— Plot of the [Fe II] 1.46 μm -to-Br- γ line ratio as a function of the CO (6-5)-to-continuum flux ratio for the NGC 5135 clumps as labelled. The extinction corrected [Fe II] and Br- γ line surface brightnesses at the local of a clump are estimated from Bedregal et al. (2009) and the typical error is 0.15 dex. The typical ratios for different types of astrophysical objects are noted in the plot (see the text). The clump *d* is not plotted here as it does not have the corresponding [Fe II] or Br- γ data.

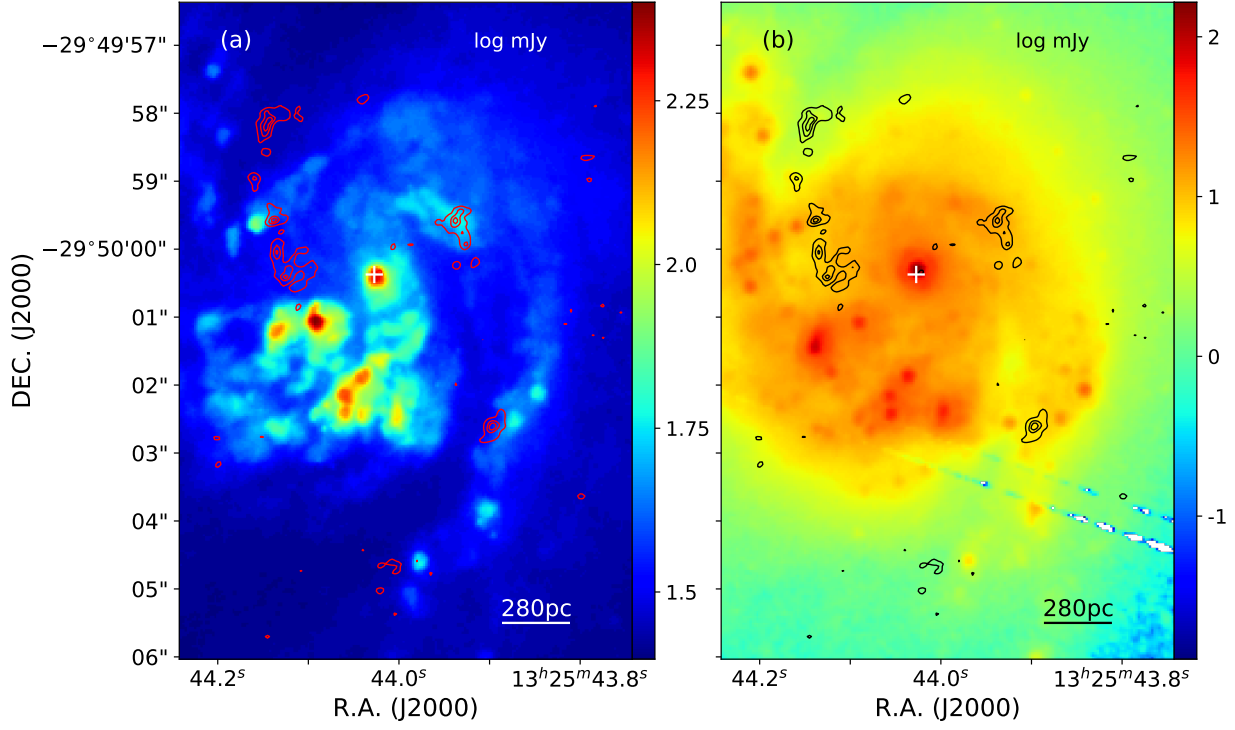


FIG. 12.— Integrated CO (6-5) line emission contours, at $[3, 5, 6] \times \sigma$ (where $\sigma = 1.2 \text{ Jy beam}^{-1} \text{ km s}^{-1}$), overlaid on (a) an *HST* F606W ($0.606 \mu\text{m}$, in log scale) image and (b) an *HST* F160W ($1.60 \mu\text{m}$, in log scale) image. The white plus sign in each panel marks the AGN position.

TABLE 2
PHYSICAL PROPERTIES OF THE INDIVIDUAL CLUMPS IN OUR CO (6-5) IMAGE

No.	Size "×"	PA Deg	Radius pc	V_0 kms ⁻¹	ΔV_{FWHM} kms ⁻¹	f_{peak} Jy beam ⁻¹ km s ⁻¹	$f_{\text{CO(6-5)}}$ Jy kms ⁻¹	I_{cont} mJy	M_{vir} ×10 ⁷ M _⊙	M_{mol} ×10 ⁸ M _⊙	M_{mol}^* ×10 ⁸ M _⊙	$R_{\text{CO/cont}}$ kms ⁻¹
(1)	(2)	(3)	(4)	(5)	(6)	(7)	(8)	(9)	(10)	(11)	(12)	(13)
a1	0.65×0.34 ±0.019×0.010	16.50	99.2 ±2.2	4062.9 ±3.0	88.0 ±7.6	13.3	91.1 ±3.0	81.8 ±8.4	37.0 ±7.4	10.5 ±2.9	12.6 ±0.4	1113.0 ±119.0
a2	0.36×0.10 ±0.025×0.012	-0.45	44.1 ±3.0	4084.4 ±3.7	63.6 ±9.2	9.2	15.5 ±3.1	11.4 ±2.7	7.6 ±2.7	1.4 ±0.5	2.1 ±0.4	1362.0 ±419.0
a3	0.40×0.25 ±0.023×0.014	0.74	62.6 ±2.9	4053.7 ±4.0	59.1 ±6.0	10.6	29.6 ±2.1	28.7 ±6.2	8.9 ±2.3	3.7 ±1.2	4.1 ±0.3	1032.0 ±236.0
a4	0.64×0.19 ±0.054×0.011	0.13	54.1 ±4.0	4047.6 ±2.4	62.6 ±7.2	9.6	28.5 ±1.8	21.6 ±2.4	9.4 ±2.7	2.6 ±0.7	3.9 ±0.2	1321.0 ±171.0
a5	0.72×0.44 ±0.023×0.022	3.38	123.9 ±4.3	4027.6 ±1.2	61.7 ±5.6	9.6	55.0 ±1.5	39.7 ±6.3	19.7 ±4.5	5.1 ±1.5	7.6 ±0.2	1850.0 ±221.0
b	0.52×0.38 ±0.028×0.026	5.09	95.7 ±4.4	4089.6 ±1.2	76.7 ±4.4	8.9	55.3 ±2.0	13.5 ±1.9	25.9 ±3.6	1.7 ±0.5	7.6 ±0.3	4084.0 ±598.0
c	0.72×0.21 ±0.025×0.007	-32.46	76.1 ±2.1	4027.8 ±1.9	69.1 ±5.0	9.4	41.8 ±2.8	48.3 ±5.9	16.0 ±2.8	6.2 ±1.7	5.7 ±0.4	866.0 ±120.0
d ^a	0.94×0.84 ±0.016×0.014	0.00	182.0 ±2.4	4067.3 ±1.7	87.3 ±4.8	30.2	69.4 ±5.5	13.0 ±3.8	66.6 ±8.4	1.7 ±0.7	9.6 ±0.8	5320.0 ±1603.0

NOTE. — The flux shown in this table is measured after the primary beam correction.

Table columns are as follows:

Col. 1: clump number(as Fig. 1a shown).

Col. 2: Major and minor axes by 2-d Gaussian fit.

Col. 3: Major axis position angle (PA; N to E).

Col. 4: The effective clump radius after a deconvolution with the ALMA beam.

($R = 1.91\sqrt{(\sigma_x \times \sigma_y)}$, where $\sigma = \text{FWHM}/2.3548$; Solomon et al. 1987)

Col. 5: The line center velocity from 1d Gaussian fit to the line profile within an elliptical aperture with radii of (major and minor axes (FWHM)).

Col. 6: The line velocity FWHM width from 1d Gaussian fit within an elliptical aperture with radii of (major and minor axes (FWHM)).

Col. 7: Clump peak surface brightness from the clump intensity map.

Col. 8: The CO (6-5) flux within an elliptical aperture with radii of (major and minor axes (FWHM)).

Col. 9: The continuum flux density within an elliptical aperture with radii of (major and minor axes (FWHM)).

Col. 10: Virial mass (see the text).

Col. 11: Molecular gas mass (estimated from the dust continuum, see the text).

Col. 12: Molecular gas mass (estimated from the CO flux, see the text).

Col. 13: Ratio of the total CO (6-5) flux to the 435 μm dust continuum flux density.

^aUsing the image in Fig. 3d, corresponding to a larger beam of 0.4" × 0.4".